Acta Pharmaceutica Sinica B 2025;15(6):3125−3148

Chinese Pharmaceutical Association
Institute of Materia Medica, Chinese Academy of Medical Sciences

Acta Pharmaceutica Sinica B

www.elsevier.com/locate/apsb
www.sciencedirect.com

ORIGINAL ARTICLE

The crucial function of IDO1 in pulmonary fibrosis: From the perspective of mitochondrial fusion in lung fibroblasts and targeted molecular inhibition

Lei Wang[a], Shanchun Ge[a], Ye Zhang[a], Deqin Feng[b], Ting Zhu[c], Louqian Zhang[d,*], Chaofeng Zhang[a,*]

[a]*Sino-Jan Joint Lab of Natural Health Products Research, School of Traditional Chinese Medicines, China Pharmaceutical University, Nanjing 210009, China*
[b]*State Key Laboratory of Microbial Resources Chinese Academy of Sciences, Beijing 100049, China*
[c]*Institute of Neuroregeneration & Neurorehabilitation, Department of Pathophysiology, School of Basic Medicine, Qingdao University, Qingdao 266021, China*
[d]*Department of Thoracic Surgery, Nanjing Drum Tower Hospital, Medical School, Nanjing University, Nanjing 210031, China*

Received 7 July 2024; received in revised form 19 August 2024; accepted 20 December 2024

KEY WORDS

Indoleamine 2,3-dioxygenase 1;
Mitochondrial dynamics;
Lipid metabolism;
Transcriptomics;
Lung fibroblasts;
Targets;
Wedelolactone;
Pulmonary fibrosis

Abstract The pathogenesis of pulmonary fibrosis (PF) is complex. It is characterized by myofibroblast hyperplasia and deposition of collagen protein. Indoleamine 2,3-dioxygenase 1 (IDO1) is expressed in lung fibroblasts and epithelial cells, but its functions in lung homeostasis and diseases remain elusive. Here, we characterize the critical role of IDO1 in PF patients and bleomycin (BLM)-induced PF mouse models. We find that IDO1 is significantly upregulated in the fibrotic lungs of patients and mice, showing a positive correlation with genes characteristic of fibrosis. Functionally, IDO1 knockout inhibits lung fibroblast proliferation, differentiation, mitochondrial biogenesis, and mitochondrial oxidative phosphorylation. Conversely, IDO1 overexpression and accumulation of kynurenine (Kyn) exacerbate progressive lung fibrosis. Mechanistically, IDO1-deletion activated profound mitochondrial fusion-enhanced potentially the capacity for fatty acid oxidation, along with activation of *de novo* glycolytic serine/glycine synthesis pathways and mitochondrial one-carbon metabolism. Wedelolactone (WEL), a small molecule IKK

*Corresponding authors.
E-mail addresses: zhanglouqian@126.com (Louqian Zhang), zhangchaofeng@cpu.edu.cn (Chaofeng Zhang).

Peer review under the responsibility of Chinese Pharmaceutical Association and Institute of Materia Medica, Chinese Academy of Medical Sciences.

https://doi.org/10.1016/j.apsb.2025.04.027

inhibitor, is found to strongly bind to IDO1 and effectively protect mice from PF in an IDO1-dependent manner. Collectively, this study characterizes a promotor role for IDO1 in PF and suggests a potential avenue of targeting IDO1 to treat lung diseases.

1. Introduction

Pulmonary fibrosis (PF) is a chronic, deadly interstitial lung disease marked by collagen and extracellular matrix (ECM) buildup within fibrotic regions, along with honeycomb alterations of the subpleural and basement membranes. The predominant form of PF is idiopathic pulmonary fibrosis (IPF), which typically has a median survival rate of 2−4 years[1]. COVID-19 survivors are particularly vulnerable to the progression of PF as a result of the confluence of SARS-CoV-2-induced inflammatory lung damage and the activation of fibrotic pathways[2]. The prevalence of fibrotic lung disease is expected to rise as a consequence of a growing epidemic of chronic respiratory illnesses stemming from environmental pollutants and shifts in climate patterns[3]. IPF is characterized histologically and radiologically as usual interstitial pneumonia[4]. The excessive activation of fibroblasts and myofibroblasts results in the deposition of extracellular matrix in the alveolar walls, causing a reduction in alveolar spaces. Current treatments for IPF mainly focus on stopping the deposition of collagen by preventing the activation of myofibroblasts. However, these interventions have demonstrated limited efficacy in achieving complete resolution of IPF, underscoring the necessity to develop innovative therapeutic approaches[1,5].

Recent research has revealed sophisticated mechanisms fibroblasts and myeloid cells employ to facilitate immune tolerance by manipulating conserved metabolic signaling pathways[6]. The aberrant metabolism of tryptophan (Trp), along with its metabolic intermediate kynurenine (Kyn), is a pathway that has garnered significant interest. Indoleamine 2,3-dioxygenase 1 (IDO1) is a metabolic enzyme that binds heme and facilitates the transformation of Trp into Kyn. Beyond its role in Trp catabolism, IDO1 is well-established for its immune-regulatory functions in mitigating excessive inflammation. IDO1 is upregulated and acts as a natural brake to the inflammatory response, including Toll-like receptor and IFN-γ signaling[7,8]. IDO1 metabolites activate β-catenin signaling, which promotes colon tumorigenesis in mice[9]. Inhibiting IDO1 with the inhibitor 1-methyl tryptophan (1-MT) in mice blocked its catalytic function, leading to heightened inflammation and worsened atherosclerosis in ApoE$^{-/-}$ mice. Additionally, research has shown that the increased expression of cyclooxygenase-2 is linked to the constitutive activation of IDO1 in human tumor[10]. Additionally, upregulation of the various inflammatory cytokines, including tumor necrosis factor-alpha, interleukin (IL)-1, and lipopolysaccharide (LPS), have the potential to stimulate the expression of IDO1 in epithelial or tumor cells[11-13]. In addition to transcriptional regulation, the expression and activity of IDO1 are also modulated at the post-translational level. Specifically, the cytokine signaling 3 suppressor facilitates the proteasomal degradation of IDO1 in dendritic cells during IL-6-induced proinflammatory conditions[14]. Moreover, the binding of endogenous nitrogen monoxide to IDO1 results in reversible inhibition of its activity[15]. The immunomodulatory effects of IDO1 have been linked to the depletion of tryptophan[16] and the generation of toxic catabolites *via* the kynurenine pathway[17,18]. Nevertheless, whether PF is implicated in IDO1-mediated immune suppression remains uncertain.

After sustaining lung damage, fibroblasts undergo a phenotypic transformation into myofibroblasts in response to stimulatory factors like transforming growth factor beta (TGF-β), and hence increased production of fibrotic markers such as α-SMA, collagen, and fibronectin[19-21]. The conversion of fibroblasts into myofibroblasts and their migratory behaviors are widely recognized as characteristic features of IPF[22]. Interestingly, Kyn is generated in lung epithelial cells that express IDO1 and, in tissue macrophages, inhibits T cell activation by interacting with and stimulating immunomodulatory aryl hydrocarbon receptors[23]. The expression of IDO1 was found to co-localize with α-SMA, a widely recognized marker of fibroblast-to-myofibroblast transition in hepatic stellate cells[24]. Considerable attention has been directed towards the role of IDO1 in oxidative stress, as it serves as a crucial rate-limiting enzyme in the production of NAD^+ through both salvage and *de novo* synthesis pathways and also plays a pivotal role in regulating gene expression in diverse metabolic syndromes and inflammatory processes[25-29]. Due to their diverse functions, mammalian IDO1 enzymes have been demonstrated to have a growing impact on numerous human diseases, including autoimmune[30], cardiovascular diseases[31], cancers[32,33], neurodegenerative disorders[34], and liver diseases[35]. The development of targeted inhibitors against IDO1 holds promise for treating these diseases. However, the involvement of IDO1 in PF and TGF-β signaling remains largely uninvestigated.

To address the existing scientific gray areas and loopholes regarding IDO1, this study aims to examine the roles of IDO1 in lung fibrosis. We analyzed the expression of IDO1 in patients with PF as well as in mice exposed to single-dose bleomycin (sBLM) and multiple-dose bleomycin (mBLM). *Ido1* knockout (KO) mice and those receiving an IDO1 inhibitor were generated to characterize the role of IDO1 in the lung fibrotic process. Spatial metabolomics, whole transcriptome sequencing, and pull-down were applied to explore the potential mechanisms IDO1 promotes lung fibrosis. Moreover, natural compounds were screened to bind to mammalian IDO1 and protect lungs from injury in mice.

2. Materials and methods

2.1. Human lung biopsy studies

This research followed the ethical standards outlined by the *Declaration of Helsinki* and secured lung biopsy samples from participants at Nanjing Drum Tower Hospital (Nanjing, China). The utilization of human lung biopsy samples in this study obtained ethics approval from the Research Ethics Committee of Nanjing Drum Tower Hospital. The ethics number for this study is No. 2020-158-2. All study participants willingly volunteered and furnished written informed consent. Studies were conducted using

human lung tissues from individuals diagnosed with PF. Control lung tissues, donated but unsuitable for transplantation, were also utilized. Five patients with lung cancer were diagnosed with PF through biopsy.

2.2. Animals

Male C57BL/6J mice, aged 8−10 weeks and weighing 18−22 g, were sourced from Bikai Biological Technology Co., Ltd. (Nanjing, China). *Ido1* KO mice, based on a C57BL/6J genetic background, were generously provided by Prof. Guo of China Pharmaceutical University (Nanjing, China). Heterozygous $Ido1^{+/-}$ mice were bred to produce $Ido1^{+/+}$ and $Ido1^{-/-}$ genotypes. The animals were kept in controlled conditions with consistent temperature, humidity, lighting, and cleanliness. The animals had unlimited access to food and water during the study. On the day of euthanasia, they were deeply anesthetized with isoflurane prior to being euthanized through decapitation. This study was rigorously adherent to the Guide for the Care and Use of Laboratory Animals and obtained ethical clearance from the Animal Experimentation Ethics Committee of China Pharmaceutical University (Approval No. SYXK (su) 2022-0012).

2.3. BLM-induced fibrosis model

Male mice were anesthetized using pentobarbital sodium and administered intratracheal sprays of BLM (Shanghai YuanYe Biotechnology Co., Ltd., Shanghai, China) dissolved in 50 μL of PBS (1 U/kg) every 14 days for a total of 8 administrations. The mice were euthanized on Day 21 and Day 42 following the final BLM challenge. The BLM model entailed a single intratracheal injection of BLM (3 U/kg), with mice being sacrificed on Day 21 and Day 42 post-injection.

2.4. In vivo wedelolactone (WEL), indoximod (1-methyl-D-tryptophan, 1 MT), and Kyn treatment

C57BL/6J mice (male, 8−10 weeks, Bikai Biological Technology Co., Ltd., Nanjing, China) underwent a single or multiple injections of BLM. In the sBLM-induced model, treatment with nintedanib (40 mg/kg; Selleck, S1010) and WEL (10 and 20 mg/kg) was administered by oral gavage daily starting from Day 14 after BLM instillation and continued the treatment for 7 days. At 14 days after administration of BLM, Kyn (20 mg/kg) was administered by intraperitoneal (i.p.) injections and continued the treatment for 7 days. For the mBLM model, mice were treated with nintedanib (40 mg/kg) and WEL (5, 10, and 20 mg/kg) starting 14 days post the final BLM challenge for 7 days, once a day by oral gavage. WT mice were administered intraperitoneal injections of either 100 mg/kg of 1 MT (Sigma−Aldrich) or 20 mg/kg of Kyn (Sigma−Aldrich) or PBS as a control on an every-other-day schedule from P1 up to P28, with a single injection of BLM on P7. *Ido1* KO mice were treated with 20 mg/kg of Kyn *via* i.p. injections, following the same every-other-day regimen from P1 to P28, and also received a single BLM injection on P7.

2.5. RNA sequencing

According to the manufacturer's guidelines, total RNA was separated and purified from lung tissue using a TRIzol reagent (Invitrogen, Carlsbad, CA, USA). Its integrity was confirmed *via* denaturing agarose gel electrophoresis. This RNA underwent fragmentation and reverse transcription into cDNA using SuperScript™ II Reverse Transcriptase (Invitrogen, cat. 1896649, USA). After these initial steps, the resultant products were PCR amplified to construct a cDNA library, which boasted an average insert size of 300 ± 50 bp. The library was sequenced using an Illumina Novaseq™ 6000 (LC-Bio, China) platform, producing paired-end reads of 2 × 150 bp in accordance with the manufacturer's instructions. The sequencing reads were aligned to the genome with HISAT2 software and assembled *via* StringTie using standard settings. All transcripts' expression levels were quantified and assessed, identifying different mRNAs with a fold change exceeding 2 or below 0.5 and a *P*-value less than 0.05 through the edgeR R package. The study concluded with a KEGG enrichment analysis to identify significantly altered pathways.

2.6. MALDI-MSI analysis

MALDI-MSI experiments were performed on an equipped Ultraflextreme MALDI-TOF MS (QuanTOF, Intelligene Biosystems, China). Freshly excised lung tissue is snap-frozen in liquid nitrogen for 10 s before being stored at −80 °C. It is then sectioned into 10 μm slices with a Leica cryostat microtome. These sections are mounted on ITO-coated conductive slides. Before MALDI-MSI analysis, the slides undergo a vacuum drying process for 45 min at room temperature.

MALDI-MSI analysis was performed in positive and negative ion modes with a nominal mass resolution of 7000 and a *m*/*z* range of 100−1000. 1,5-Diaminonaphthalene hydrochloride served as the spray solvent, and a uniform matrix layer was sprayed on lung tissue sections using an automated matrix sprayer (HTX Technologies™). In positive and negative ion mode, the transport tube voltage is set to 2000 and −1500 V, respectively, and the nebulizer voltage is set to 7500 and −4500 V, respectively. The pumping flow rate was set at 45 L/min. The MSI experiment continuously scans the surface of the lung tissue section at a constant rate of 200 μm/s in the *x*-direction and vertically at 200 μm in the *y*-direction.

2.7. Transmission electron microscopy (TEM)

The ultrastructural changes in mitochondria from three mice per group were observed using TEM 21 days post-BLM. Following euthanasia, the lungs were promptly excised from the mice and rinsed with ice-cold 0.9% NaCl. Using glutaraldehyde buffer and OsO_4, 1 mm^3 lung cubes were fixed. Ultrathin sections were prepared, stained with lead citrate and uranyl acetate, and subsequently analyzed using a JEM1400 TEM from JEOL, Tokyo, Japan.

2.8. Plasmid construction

The cDNA sequences encoding human and mouse IDO1 were successfully cloned into a pCMV-HA vector, each featuring a FLAG-HA tag sequence at the N-terminal region. For the IDO1 expression vector, the full-length cDNA of mouse IDO1 was also inserted into the same pCMV-HA expression system. The sequences used for this purpose were obtained from NCBI.

2.9. Fibroblast isolation and culture

Primary mouse lung fibroblasts (MLFs) were isolated from 8-week-old WT and *Ido1* KO mice. The process started with flushing the mouse lungs with PBS, then rinsing with ice-cold HBSS-Ca/Mg. The lung tissues were subsequently finely minced

with sterilized scissors. The tissues were finely minced and subjected to enzymatic digestion at 37 °C for 1 h using a buffer solution containing collagenase (0.5 mg/mL) and trypsin (0.5 mg/mL) in HBSS-Ca/Mg. After digestion, the tissue underwent filtration using a 70-μm cell strainer to isolate the cells, which were subsequently collected *via* centrifugation at 800 × *g* for 5 min. The cell pellets obtained were cultured in high-glucose Dulbecco's modified Eagle's medium (DMEM) supplemented with 10% fetal bovine serum (FBS, Gibco) and then seeded onto culture dishes. Fibroblast cells attach more quickly than epithelial cells, so seeded cells were allowed to attach for 2−4 h before washing with PBS and adding fresh growth medium. Once cells reached 80% confluency, the cells were subcultured. The purity of isolated fibroblasts was verified by positive immunostaining for vimentin, fibronectin, and collagen type I.

Primary human lung fibroblasts (HLFs) were obtained from lung tissues of healthy donors deemed unsuitable for transplantation ($n = 5$). The Ethics Committee of Nanjing Drum Tower Hospital approved the research protocol, and written informed consent was obtained from all donors before tissue collection. In Brief, lung tissue samples were finely minced and underwent enzymatic dissociation using Hank's balanced salt solution supplemented with 600 U/mL collagenase I, 2 U/mL protease, 2 U/mL papain, and 3.8 mmol/L calcium chloride at 37 °C for 1 h. The dissociated tissues were gently triturated using a glass pipette, followed by centrifugation of the resulting cell suspension at 800 × *g* for 5 min to collect the cells. The collected cells were resuspended in high-glucose DMEM supplemented with 10% FBS, 50 U/mL streptomycin, and 50 μg/mL penicillin. HLFs were affirmed by positive immunocytochemistry for vimentin. HLFs were cultivated and used in the third to sixth passage.

2.10. Cell culture, transfection, and treatment

MLFs and HLFs were grown in a medium containing high-glucose DMEM and 10% FBS. MLFs and HLFs were treated with WEL (5, 2.5, and 1 μmol/L) for 24 h and stimulated with TGF-β (10 ng/mL) for 24 h.

To confirm that IDO1 inhibition effectively alleviates the differentiation of the lung fibroblasts. According to the manufacturer's protocol, the IDO1 plasmids were transfected into MLFs and HLFs with JetPrime (Polyplus, France).

For IDO1 affect mitochondrial fission and fusion test, The MLFs were isolated from WT or *Ido1* KO mice and subsequently treated with TGF-β (10 ng/mL) for 24 h wild-type IDO1 plasmid or IDO1 mutant plasmid was transfected to the primary lung fibroblasts derived from *Ido1* KO mice separately.

2.11. Modified WEL synthesis

WEL dry powder was first dissolved in DMSO and HCl to adjust the pH to 6.0. Carboxymethyl hydroxylamine was then added to derive the carboxyl groups, which were activated using EDC/NHS. The BSA was dissolved in distilled water, followed by a pH adjustment to 9.5 using $NaHCO_3$. This solution was then linked to WEL−NHS, FITC, and biotin. The mixture was shielded from light for 2 h, centrifuged to remove any denatured protein, and dialyzed to eliminate free small molecules, resulting in the BSA−WEL−FITC−biotin complex. The complex was quantified and collected after a final round of centrifugation and concentration.

2.12. Biotin-WEL pull-down assay

Pull-down assays were used to identify the protein target of WEL. The Sepharose® Bead Conjugate (CST, #3419) was employed to conjugate WEL. MLF lysates are treated with WEL-biotin or WEL and shaken overnight at 4 °C. Proteins captured by the beads were rinsed five times using PBS, after which a loading buffer was added, and the mixture was boiled for 10 min. Subsequently, separation was achieved using 10% SDS-PAGE, followed by analysis through Western blotting.

2.13. Wound healing assay

Wound healing assays were conducted using HLFs and MLFs. The MLFs were isolated from WT or *Ido1* KO mice. The Flag-tagged IDO1 overexpression plasmid and the corresponding control plasmid were transfected into HLFs. After reaching total growth in 12-well plates, the cells were deprived of nutrients in an FBS-containing medium for 6 h. Wounds were inflicted on the cell layers reached confluence by a 200 μL sterile pipette tip. Following a wash with PBS, the cells were cultured in a medium containing TGF-β (10 ng/mL) at 37 °C and 5% CO_2 for 24 h.

2.14. Mitochondrial oxygen consumption rate (OCR) analysis

The Seahorse XFe96 Extracellular Flux Analyzer (Agilent Technologies) was employed to assess the glycolytic and mitochondrial oxidative phosphorylation (OXPHOS) rates in primary lung fibroblasts. These cells, derived from the lungs of WT and *Ido1* KO mice, underwent a 24 h stimulation with TGF-β. MLFs were seeded at 4×10^5 cells per well for further analysis. The OCR for each well was examined utilizing the XF Cell Mito Stress Test, which included administering a series of compounds at precise concentrations: 10 mmol/L glucose, 2 μmol/L oligomycin, 50 mmol/L 2-deoxy-D-glucose, 1 μmol/L FCCP, and 0.5 μmol/L rotenone/antimycin A. The necessary kit for this test was sourced from Agilent Technologies, Inc.

2.15. Carboxy-fluorescein succinimidyl ester (CFSE) cell proliferation assay

Cell proliferation was evaluated using CFSE staining. Initially, cell pellets were resuspended in phosphate-buffered saline (PBS) containing 0.1% bovine serum albumin (BSA) and labeled with 5 μmol/L CFSE for 10 min at 4 °C. After labeling, Samples were chilled using an ice-cold medium for 5 min and subsequently rinsed twice with PBS. Following washing, the cells were cultured in dishes and received the necessary treatments. A Beckman Coulter CytoFLEX S flow cytometer then measured the fluorescence intensity.

2.16. Cellular thermal shift assay (CETSA)

Cell lysates were exposed to WEL (5 μmol/L) for 30 min at 4 °C, followed by experiments at temperatures ranging from 42 to 82 °C for 3 min. The supernatants obtained from centrifugation were subsequently subjected to Western blot analysis using the IDO1 antibody, with a vehicle serving as the control group in these experiments.

2.17. Drug affinity responsive target stability (DARTS)

Cell lysates were treated with WEL at concentrations of 2.5, 5, and 10 μmol/L for a period of 1 h, followed by Pronase E (5 μg/mL; Sigma−Aldrich) treatment for 30 min. The supernatants were then analyzed *via* Western blot using the IDO1 antibody, with a vehicle used as the control group.

2.18. MMP analysis

After treatment, add JC-1 working solution (10 μg/mL) to the cells and incubate at 37 °C in a 5% CO_2 environment for 30 min. Following this, the cells should be washed three times with PBS, with each wash lasting 2 min. Images can then be captured using a fluorescence microscope (LSM700, Carl Zeiss, Germany), with the excitation and emission wavelengths adjusted to 514 nm and 590 nm, respectively.

2.19. Mito-tracker staining assay

Cells will be cultivated in confocal dishes for 24 h, after which they will be treated, and a Mito-tracker working solution (200 nmol/L) will be applied. This is followed by an incubation period of 30−45 min at 37 °C in a 5% CO_2 atmosphere. Fluorescence microscopy (LSM700, Carl Zeiss, Germany) will then capture images, utilizing emission wavelengths and excitation of 490 and 516 nm, respectively.

2.20. Content of hydroxyproline in vivo

Briefly, the samples underwent hydrolysis with hydrochloric acid followed by centrifugation at 12,000 × *g*. Chloramine-T oxidized hydroxyproline in the samples, adding perchloric acid to remove the chloramine-T. Subsequently, the oxidized samples were then exposed to 4-(dimethylamino) benzaldehyde to produce a compound measurable photometrically at 560 nm. Data were collected using a plate reader and analyzed based on the hydroxyproline standard curve provided with the assay kit.

2.21. Content of malondialdehyde (MDA) in vivo

The serum MDA concentration was analyzed using assay kits sourced from the Nanjing Jiancheng Bioengineering Institute. The provided instructions determined the MDA levels according to the manufacturer's guidelines for preparing the working solution.

2.22. Immunofluorescence staining

In examining lung samples, sections were permeabilized with 0.1% Triton X-100 and blocked with 5% BSA in PBS for 20 min at room temperature. Subsequently, the sections were exposed to primary antibodies overnight at 4 °C, followed by treatment with fluorescently labeled secondary antibodies. DAPI was used for counterstaining the slides. We then analyzed and imaged the samples using the pathological section scanner (HS6, SUNNY).

In examining the colocalization of WEL and IDO1, cells were cultured in 6-well plates and exposed to either WEL−FITC−biotin or a control vehicle for 6 h. Following fixation, the cells were incubated overnight with the primary IDO1 antibody at 4 °C, followed by a 1-h incubation with a fluorescent secondary antibody. Colocalization was assessed utilizing fluorescence microscopy (LSM700, Carl Zeiss, Germany).

2.23. Histologic examination and immunohistochemical staining

Lung tissue sections were subjected to fixation using 4% paraformaldehyde at room temperature overnight, subsequently undergoing staining with HE and Masson's trichrome. The fibrotic extent was evaluated based on the Ishak scoring system[36].

The lung tissue underwent fixation in 4% paraformaldehyde, was then embedded in paraffin, deparaffinized, rehydrated through an ethanol series, and stained *via* the peroxidase anti-peroxidase technique. For antigen retrieval, sections were boiled in a 10 mmol/L citric acid solution (pH = 6) or a 1 mmol/L EDTA and 10 mmol/L Tris solution for 20 min (pH = 9). After blocking endogenous peroxidase activity with 3% hydrogen peroxide, the sections were incubated overnight at 4 °C with the primary antibody, followed by the appropriate secondary antibody. For visualization, 3,3′-diaminobenzidine (DAB) was used as the chromogen. After counterstaining with hematoxylin, sections were dehydrated, mounted with coverslips, and imaged using the AxioScan.Z1 fully automated slide scanner (Zeiss, Jena).

2.24. Reverse-transcription PCR (RT-PCR)

Total RNA was isolated with Trizol (Invitrogen), reverse transcribed with iScriptTM cDNA Synthesis Kit (NUOWEIZAN, Nanjing, China), and amplified in triplicate using iQTM SYBR Green Supermix kit and CFX96 Real-Time System (Bio-Rad Laboratories). Data were analyzed using the $2^{-\Delta\Delta CT}$ method with specific primer sequences listed in Supporting Information Table S1.

2.25. Western blots

Lysates and protease inhibitors extract proteins in tissues or cells. Samples placed with magnetic beads were homogenized and centrifuged (14,000 rpm, 10 min, 4 °C). With the normalization of concentration by using a BCA kit, the quantified protein was added to the SDS-PAGE loading buffer and boiled to denaturation, stored at −20 °C until use. An equal amount of protein from each sample was run in 10%−12 % Tris-glycine SDS-PAGE gel at 70 V for ∼1 h, then transferred to the NC membrane. After blocked with 5% skim milk, protein-loaded membranes were probed with primary antibodies at 4 °C overnight, followed by incubation with horseradish peroxidase conjugated anti-IgG. The secondary antibody was applied for 1 h at room temperature, and protein visualization was done using ECL.

2.26. Antibodies

The primary antibodies used were as follows: anti-IDO1 (CST, #51851, 1:1000 for IB), anti-IDO1 (CST, #86630, 1:1000 for IB, 1:200 for IHC), anti-IDO1 (Santa Cruz, sc-137012, 1:100 for IB, 1:50 for IF, and 1:50 for IHC), anti-HAAO (Proteintech, 12791-1-AP, 1:1000 for IB), anti-kynureninase (Santa Cruz, sc-390360, 1:100 for IB), anti-KMO (Proteintech, 60029-1-Ig, 1:5000 for IB), anti-QAPRTase (Santa Cruz, sc-100809, 1:200 for IB), anti- α-SMA (CST, #19245, 1:1000 for IB, 1:200 for IHC, 1:200 for IF), anti-E-cadherin (CST, #14472, 1:1000 for IB, 1:200 for ICH), anti-Fibronectin (Santa Cruz, sc-8422, 1:50 for IHC), anti-Vimentin (CST, #5741, 1:1000 for IB), anti-collagen I (CST, #72026, 1:1000 for IB, 1:200 for ICH), anti-PGC1a (Proteintech, 66369-1-Ig, 5000 for IB), anti-SDHB (Santa Cruz, sc-271548,

1:100 for IB), anti-NDUFB8 (Proteintech, 14794-1-AP, 5000 for IB), anti-UQCRC2 (Proteintech, 14742-1-AP, 2000 for IB), anti-MTCO2 (Proteintech, 55070-1-AP, 2000 for IB), anti-ATP5A1 (Proteintech, 14676-1-AP, 5000 for IB), anti-DRP1 (CST, #8570, 1:1000 for IB), anti-FIS1 (Proteintech, 10956-1-AP, 1000 for IB), anti-Mff (Santa Cruz, sc-398617, 1:100 for IB), anti-OPA1 (Abcam, ab42364, 1:1000 for IB), anti-OPA1 (Proteintech, 27733-1-AP, 1:1000 for IB), anti-OPA1 (Santa Cruz, sc-393296, 1:50 for IF), anti-Mfn2 (Abcam, ab124773, 1:1000 for IB), anti-MFN1 (Proteintech, 13798-1-AP, 2000 for IB, 1:200 for IF), anti-Hsp60 (Abcam, ab190828, 1:1000 for IB), anti-Tim17 (Santa Cruz, sc-271152, 200 μg/mL for IB), anti-SOD2 (Santa Cruz, sc-137254, 200 μg/mL for IB), anti-TOM20 (Proteintech, 11802-1-AP, 1:2000 for IB), anti-fatty acid synthase (Abcam, ab128870, 1:10,000 for IB, 1:250 for IF). PPARγ (Santa Cruz, sc-7273, 1:50 for IHC). PPARγ2 (Abcam, EPR25862-79, 1:200 for IHC). anti-GAPDH (CST, #2118, 1:1000 for IB), anti-β-actin (Abcam, ab8226, 1:1000 for IB), DYKDDDDK tag Polyclonal antibody (Binds to FLAG® tag epitope) (Proteintech, 20543-1-AP, 1:20,000 for IB).

Anti-rabbit IgG, HRP-linked antibody (CST, #7074, 1:3000 for IB), anti-mouse IgG, HRP-linked antibody (CST, #7076, 1:3000 for IB), Alexa Fluor 488 goat anti-rabbit IgG (Abcam, ab150077, 1:200 for IF), Alexa Fluor 594 goat anti-mouse IgG (CST, #8890, 1:1000 for IF).

2.27. Molecular dynamics stimulation

The Gromacs 2019 simulation software was used to perform molecular dynamics simulations, with the SPC water model applied to simulate water molecules within the OPLS2005 force field accurately. Counter ions were introduced and evenly spread across the solvated system to ensure charge neutrality. The system underwent minimization following Desmond's established protocol before beginning the molecular dynamics simulations. Temperature and pressure were consistently maintained at 300 K and 1 atm, respectively, using the Nose−Hoover thermostat. This preparation enabled the completion of 100 ns of continuous NPT molecular dynamics simulations without any constraints.

2.28. Statistical analysis

Statistical analyses were conducted with GraphPad Prism 8. Differences among groups were analyzed using one-way or two-way ANOVA, followed by Tukey's tests as needed. Unpaired *t*-tests were utilized to compare the two groups. Results are presented as mean ± standard deviation (SD) or numbers (percentages) for categorical variables. All tests were two-sided, with $P < 0.05$ deemed to indicate statistical significance.

3. Results

3.1. IDO1 expression was elevated in the fibrotic lung tissues of IPF patients

Initially, we analyzed the expressions of the three key enzymes in the kynurenine pathway (KP) (*IDO1*, *IDO2*, *TDO2*) using the NCBI Gene Expression Omnibus database (http://www.ncbi.nlm.nih.gov/geo/). In the NCBI's Gene Expression Omnibus database (GSE124685), the mRNA of *IDO1* but not *IDO2* and *TDO2* was markedly increased in the biopsy lung tissue of patients with PF ($n = 154$) compared with that in control subjects ($n = 20$) (Fig. 1A). *IDO1*, *IDO2*, and *TDO2* transcript expression levels were examined in the lung tissues of both control subjects and PF patients. *IDO1* and *IDO2* mRNA significantly increased, whereas no change in *TDO2* mRNA levels was found in the lungs of IPF patients (Fig. 1B). Following this lead, we examined the indices of fibrosis and their correlation with IDO1 expression. The findings revealed significantly increased mRNA expressions of *COL1A1*, *COL3A1*, *ACTA2*, *VIM*, and *TGFB1* in the fibrotic lung compared to the control group (Supporting Information Fig. S1A). Notably, these fibrosis indices were positively correlated with the expression of IDO1 (Fig. S1B−S1F).

Next, we examined 10 microdissected human lung samples, which included specimens from patients diagnosed with PF ($n = 5$) and those without any PF or specific pathological alterations as determined by biopsy procedures ($n = 5$). Patients with PF exhibited severe lung injury and collagen deposition as described by Masson and hematoxylin−eosin (HE) staining (Fig. 1C−E, and F). Immunohistochemistry (Fig. 1C and D) and immunofluorescence (Fig. S1G and S1H) showed that IDO1 protein expression was strikingly higher in PF patients than in control subjects. Also, IDO1 expression exhibited a robust positive association with the lung injury score (Fig. 1G). Western blots showed that upregulation of IDO1 protein expression in the lungs of IPF patients was also indicated (Fig. 1H). Immunofluorescence displayed that increased expression of IDO1 was principally co-localized with α-SMA, a biomarker for fibroblast conversion in PF (Fig. 1I−K).

3.2. Increased IDO1 expression and abnormal Kyn metabolic pathway were detected in BLM-induced PF mice

To explore the pathological evaluation of PF, a PF mouse model was created through the administration of sBLM and mBLM. Our study revealed that mice treated with sBLM exhibited notable fibrotic lesions by Day 21 following injury, but these lesions had resolved by Day 42 post BLM instillation. In contrast, mice treated with mBLM displayed persistent PF lesions and collagen deposition throughout the study period (Supporting Information Fig. S2A−S2H). Subsequently, RNA-seq was conducted to examine the transcriptome of wild-type (WT) mouse lungs, both untreated and treated with mBLM. Transcriptional analysis illustrated that the extensively upregulated critical genes involved in Trp metabolism (Fig. 2A). This result was consistent with human studies (Fig. S1I). Volcano plots of differentially expressed genes in WT and mBLM-treated WT mouse lungs also revealed an overwhelming dependency of mBLM-induced transcriptomic changes on critical genes involved in Trp metabolism (Fig. 2B).

Next, we determined the expression of key enzymes implicated in KP. Quantitative immunoblot analysis revealed significant elevations in the levels of the KP enzymes, including IDO1, 3-hydroxy anthranilate 3,4-dioxygenase (HAAO), kynurenine-3-monooxygenase (KMO), kynureninase (KYNU), and QPRT in the lungs of the fibrotic mice (Fig. 2C and D). The lungs of the fibrotic mice also exhibited significantly increased mRNA of *Ido1* and *Kmo* (Fig. 2E). sBLM or mBLM-induced PF displayed extensive collagen deposition and lung injury as evidenced by Masson (Supporting Information Fig. S3A, S3C, S3D, and S3F) and HE staining (Fig. S3A, S3B, S3D, and S3E). Immunohistochemistry (Fig. S3A, S3D, S3G, and S3H) and immunofluorescence (Fig. S3I) analyses demonstrated a notable elevation in IDO1 protein levels in mice exhibiting PF compared to those in a

non-fibrotic state. Also, there was a marked positive association between the levels of IDO1 and the severity of lung injury (Fig. S3J and S3K). Immunofluorescence analysis revealed a significant co-localization of increased IDO1 content with α-SMA (Fig. S3L and S3M).

The studies above demonstrated that the related enzymes involved in the Kyn pathway were upregulated. These findings motivated us to investigate further the impact of PF on the generation of KP metabolites. WT mice were subjected to either saline or BLM treatment, and their lungs were collected 24 h after Day 21 post-treatment. After euthanasia and lung dissection, histopathological staining with HE and matrix-assisted laser desorption/ionization mass spectrometry imaging (MALDI-MSI) were conducted on the lungs of both groups of mice (Supporting Information Fig. S4A). We conducted metabolic analysis in the regions of the total lung tissues between both BLM and saline-treated WT mice (Fig. S4B). We observed significant increases in Trp, L-Kyn, 3-hydroxyanthranillc acid, quinolinic acid in lung tissues of mice exposed to BLM compared to controls and the spatial distribution also changes. 3-Hydroxyl kynurenine did not significantly differ, which may have arisen from the high variance of 3-HK levels in the BLM group and the relatively small number of animals (Fig. 2F and G).

3.3. IDO1-deletion mediated Kyn insufficiency inhibits PF

To examine the involvement of IDO1 in the pathogenesis of PF, we employed the CRISPR-Cas9 technique to create *Ido1* KO mice. IDO1 knockout was verified through PCR and Western blot analysis (Supporting Information Table S2). In response to BLM (Fig. 3A), IDO1 knockout resulted in a significant decrease in mortality (Fig. 3B), ameliorated pathologic injury in the lung (Fig. 3C, D, and I), reduced collagen deposition (Fig. 3E and L), improved morphology (Fig. 3F). In addition, serum MDA and hydroxyproline (HYP) contents of *Ido1* KO mice was significantly reduced relative to WT mice (Fig. 3G and J). The Western blotting results revealed an upregulation of the epithelial cell marker E-Cadherin and a downregulation of the myofibroblast marker α-SMA and mesenchymal cell marker Vimentin in *Ido1* KO mice (Fig. 3H and K). This EMT progression was suppressed by IDO1 knockdown. Consistent with that, immunohistochemistry revealed α-SMA, collagen I, and fibronectin were dramatically suppressed in the lungs of *Ido1* KO mice (Fig. 3M−O).

As IDO1 effectively metabolized Trp to Kyn, we examined whether accumulated Kyn could cause PF. First, we suppressed Kyn synthesis by administering an IDO1 inhibitor (1 MT) at P1, followed by BLM instillation at P7. Lung tissue injury and fibrosis were detectable at P28 (Fig. 4A). As in the study of *Ido1* KO mouse, the mouse treated with 1-MT also ameliorated pathologic injury in the lung (Fig. 4B−E) and reduced collagen deposition (Fig. 4F). Subsequently, we investigated if Kyn administration may exacerbate PF when BLM instillation was carried out at P7 (Fig. 4G). At P28, mice treated with Kyn demonstrated a bulkier fibrosis area and more severe lung tissue damage than those treated with saline (Fig. 4H−L). To further assess the impact of administered Kyn on the fibrotic stage, at 14 days after administration of BLM, Kyn (20 mg/kg) was administered by intraperitoneal injections and continued the treatment for 7 days. We observed that mice treated with Kyn demonstrated a bulkier fibrosis area and more severe lung tissue damage than those treated with saline (Supporting Information Fig. S5A−S5F). In addition, *Ido1* KO mice were treated with Kyn, followed by BLM instillation to explore this aspect (Supporting Information Fig. S6A). The results showed that administering Kyn to *Ido1* KO mice exhibited more severe lung tissue damage (Fig. S6B, S6C, and S6H) and a bulkier fibrosis area (Fig. S6D and S6I) and higher levels of the EMT markers when compared with *Ido1* KO mice treated with BLM (Fig. S6E−S6G, S6J−S6L). Giving Kyn to *Ido1* KO mice nullified the protective effects of removing IDO1. This data suggests that the Kyn level increase leads to, or at least exacerbates, the development of PF and negatively impacts functional recovery of the lung to injury.

3.4. IDO1-deletion alleviated PF by regulating mitochondrial dynamics and bioenergetics

To examine the mechanisms by which IDO1 contributes to PF, we conducted RNA-seq analysis on the transcriptome of mBLM-treated WT and *Ido1* KO mouse lungs. RNA-seq analysis of mBLM-treated WT and *Ido1* KO mouse lungs revealed 556 genes with increased expression and 447 genes with decreased expression (according to $\log_2$-fold change >1 and Q value < 0.05; Fig. 5A). Subsequent comparative analysis of KEGG and GO pathways indicated a significant enrichment of mitochondrial metabolic pathways among the differentially expressed genes. In particular, oxidative phosphorylation, ABC transporters, Purine metabolism (Fig. 5C), mitochondrial respiratory chain complex I, and mitochondrial respiratory chain complex I assembly (Fig. 5D) were the top enriched KEGG pathways and GO terms.

Consistent with the KEGG and GO analysis, significant alteration of mitochondrial respiratory electron transport chain (ETC) genes was found in lungs between mBLM-treated WT and *Ido1* KO mice (Fig. 5B). Concomitantly, In the lungs of *Ido1* KO mice, we noted a significant upregulation of genes linked to mitochondrial fusion and a marked downregulation of genes associated with mitochondrial fission (Fig. 5E). Meanwhile, mitochondrial ultrastructure was evaluated through transmission electron microscopy, revealing that mitochondrial morphology was normal in WT and *Ido1* KO mouse lungs. IDO1 deletion improved mitochondrial morphology and increased mitochondrial numbers in a BLM-induced PF model compared with WT mice (Fig. 5F and G). We evaluated the protein expression of mitochondrial dynamics and bioenergetics *in vivo*. Consistent with expectations, the expression of several ETC complex proteins was a widespread increase in the lungs of *Ido1* KO mice compared to WT mice (Fig. 5H and L). Mitochondrial fusion proteins OPA1 and Mfn1 were higher in *Ido1* KO mice. DRP1 and Mff that were involved in the fragmentation of the mitochondrial network were markedly down-regulated in *Ido1* KO mice, whereas Fis1 protein levels were unaltered (Fig. 5I and K). In addition, Hsp60, SOD2, and TIM17 proteins involved in mitochondria quality control were markedly upregulated in *Ido1* KO mice, whereas Tom20 protein levels were unaltered (Fig. 5J and M). Moreover, similar to *Ido1* KO mouse lungs, 1 MT-treated lungs displayed decreased area with positive staining for α-SMA and Vimentin and increased area with positive staining for mitochondrial dynamics-related proteins Mfn1 and OPA1 (Supporting Information Fig. S7A and S7C). Conversely, mice administered Kyn demonstrated a larger fibrosis area, lower levels of OPA1 and Mfn1, and exacerbated lung injuries (Fig. S7B and S7D). Overall, these data suggest that IDO1 deletion improved mitochondrial dynamics and bioenergetics in a murine lung fibrosis model.

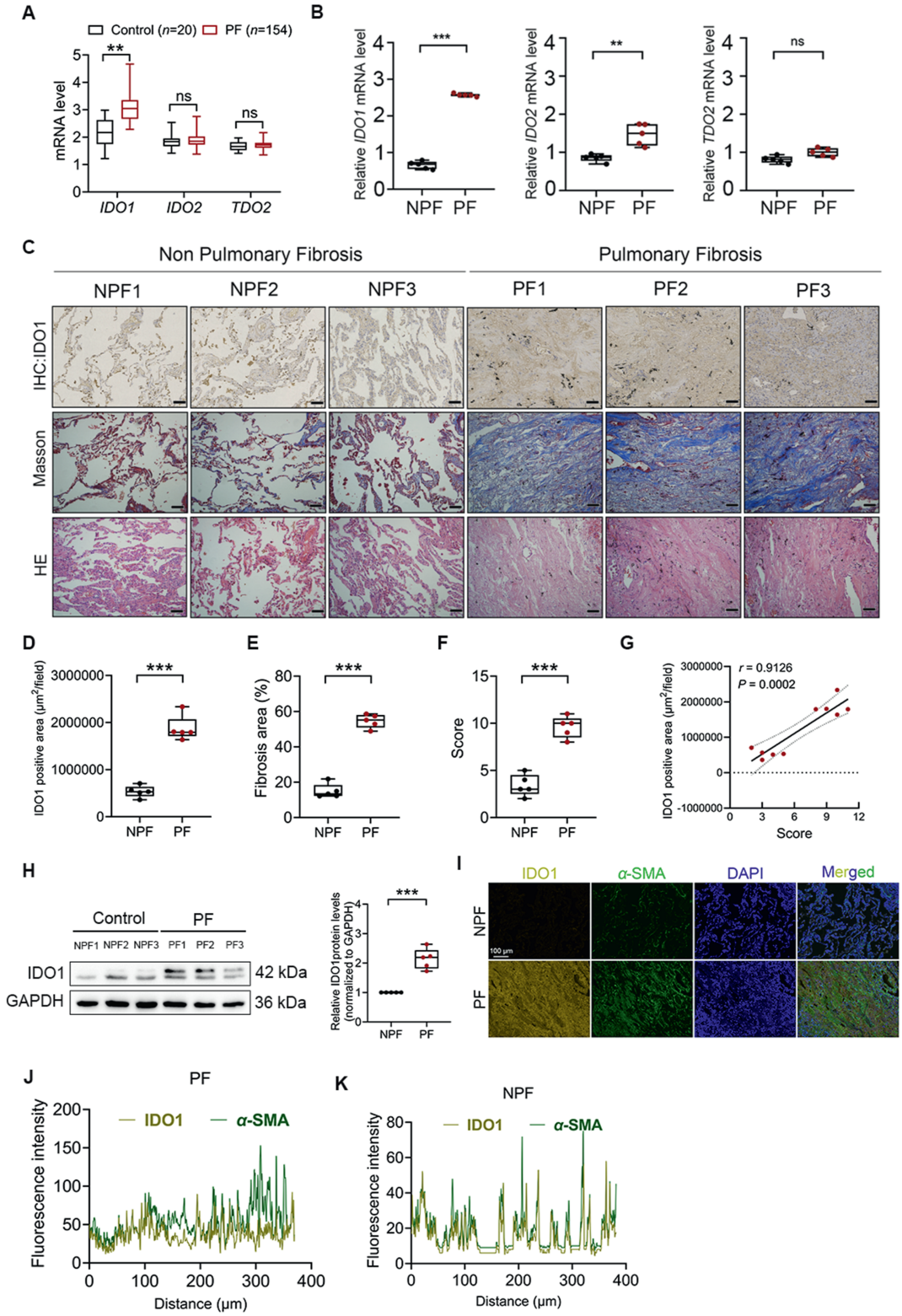

Figure 1 IDO1 is significantly upregulated in the lungs of patients with IPF. (A) Relative *IDO1*, *IDO2*, *TDO2* mRNA levels. All RNA-seq data are available in NCBI's Gene Expression Omnibus (GSE124685). $n = 20$ samples in control group, $n = 154$ samples in IPF group. Unpaired *t*-test. ns, no significant difference. (B) Relative *IDO1*, *IDO2*, *TDO2* mRNA levels in the lungs from patients with non-lung or lung fibrosis. $n = 5$ samples per group. (C) Tissue adjacent lung sections from patients with non-lung or lung fibrosis by immunohistochemistry, Masson sdtaining, and HE staining. Scale bar = 20 μm. NPF non-lung fibrosis, PF Lung fibrosis. $n = 5$ samples per group. (D–F) Quantification of IDO1 expression (D), fibrotic area (E), and score of lung damage (F) based on immunohistochemistry, Masson, or HE staining in (C). Data are presented as mean ± SD. $n = 5$ samples per group. (G) The correlation of IDO1 expression and the extent and severity of pulmonary damage ($n = 10$,

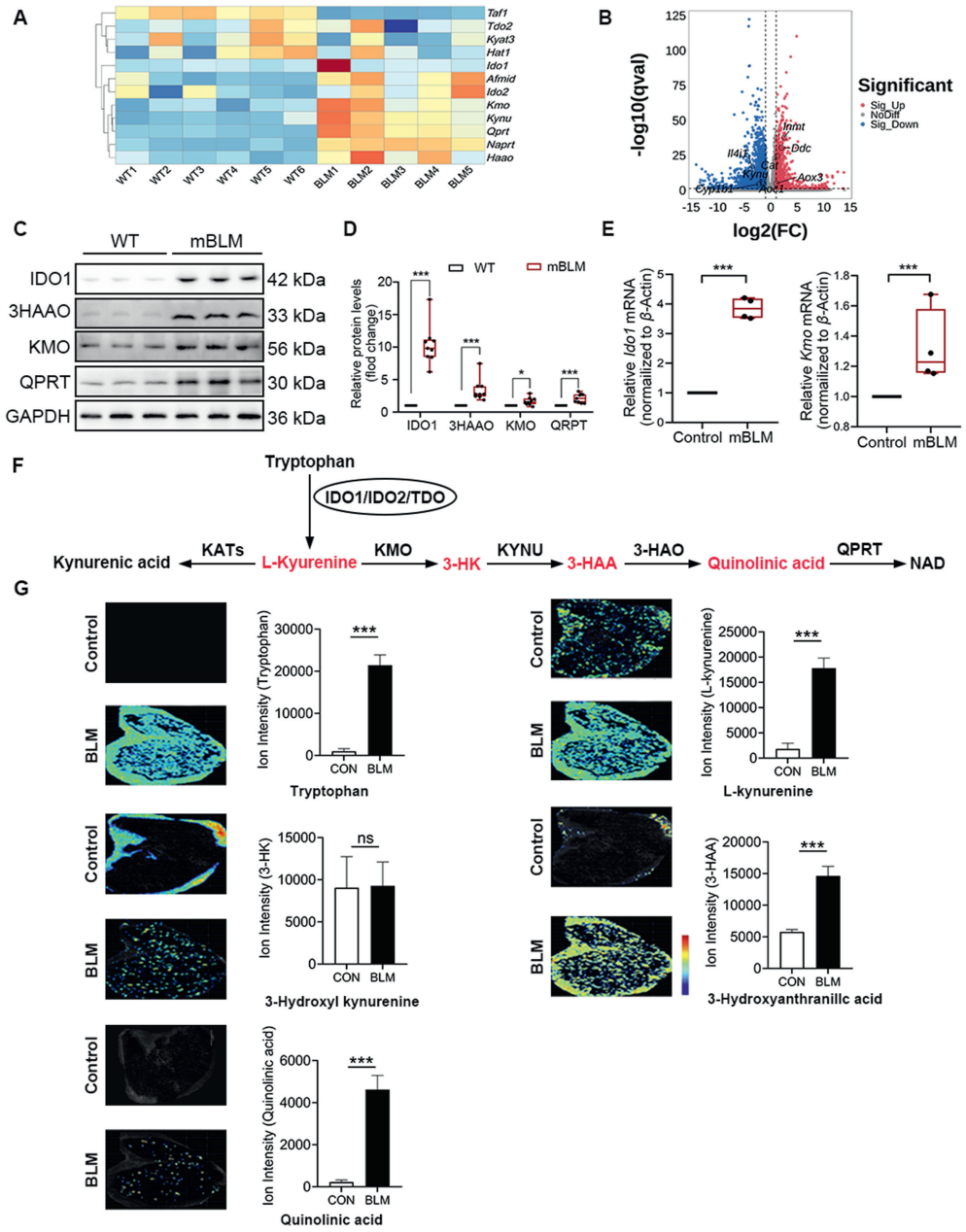

Figure 2 BLM-induced PF mice expressed increased IDO1 and displayed abnormal kynurenine metabolism. (A) Heatmap showing differentially expressed tryptophan catabolism genes in WT and mBLM-treated WT mouse lungs at 8 weeks of age ($n = 6$ WT, $n = 5$ mBLM-treated WT). (B) Different genes were regulated by mBLM treatment, as shown by RNA-seq in the volcano plot. (C) Representative immunoblot of independent experiments measuring KP enzymes in WT and mBLM-treated WT mouse lungs. (D) Quantification of KP enzyme levels normalized to GAPDH; Data are presented as mean ± standard deviation (SD), $n = 9$; $^{*}P < 0.05$, $^{**}P < 0.01$, $^{***}P < 0.001$. (E) Relative *Ido1*, *Kmo* mRNA levels in the lungs from WT and mBLM-treated WT, $n = 4$. (F) Schematic of metabolites and genes of the kynurenine pathway. (G) MALDI-MSI of metabolites involved in KP metabolism in the lungs in mice in the control and lung fibrosis groups, $n = 3$. All data are presented as mean SD, one-way ANOVAwith Turkey's multiple-comparison test, $^{*}P < 0.05$, $^{**}P < 0.01$, $^{***}P < 0.001$, ns = non-significant.

Pearson χ^2 test). (H) Relative IDO1 protein expression in the lungs from non-lung or lung fibrosis patients. $n = 3$ samples per group. (I) Representative images of IDO1 and α-SMA co-immunofluorescence staining in lung tissues of non-lung fibrosis and lung fibrotic patients. (J, K) Fluorescence intensity of IDO1 and α-SMA in diagram k-up and k-down, Image J software was used for statistics. Scale bars = 20 μm. $n = 5$ samples per group. Data are presented as box-and-whisker plots. The solid line inside the box indicates the median, the bottom and top of the box represent the first and third quartiles, and the bottom and top whisker show the minimum and maximum, respectively. All data are presented as mean ± SD, one-way ANOVA with Turkey's multiple-comparison test, $^{*}P < 0.05$, $^{**}P < 0.01$, $^{***}P < 0.001$, ns = non-significant.

3.5. IDO1-deletion significantly inhibited the proliferation and differentiation of the lung fibroblasts

MLFs and HLFs were stimulated with TGF-β, the most commonly utilized stimulating agents to induce fibrosis, to investigate the involvement of IDO1 in the pathogenesis of PF. We employed extracellular flux analysis to monitor mitochondrial respiratory capacity *in vitro*. TGF-β sharply decreased the mitochondrial respiratory capacity, including basal, maximal, and spare respiration. Conversely, IDO1 knockdown restored mitochondrial respiratory capacity (Fig. 6A and B). Mito-tracker staining analysis was conducted to investigate the potential influence of IDO1 on mitochondrial dynamics. We observed that TGF-β stimulation caused mitochondrial fission and fragmentation; this stimulation process, however, was markedly improved by IDO1 deletion (Fig. 6C). To examine the impact of IDO1 knockdown on cell proliferation, we analyzed cell cycle distribution following IDO1 knockdown using flow cytometry. The knockdown of IDO1 exhibited a marked increase in the accumulation of cells in the G0/G1 phase in MLFs, decreasing the S and G2/M phases significantly (Fig. 6D and E). The findings of a wound-healing assay indicated that the deletion of IDO1 impeded the migratory capacity of MLFs (Fig. 6F and H). To understand whether IDO1 acts on HLFs, we constructed an IDO1 plasmid to successfully enhance IDO1 expression in HLFs. The results indicated that IDO1 enhanced the migratory ability of HLFs (Fig. 6G and I). In addition, RT-qPCR evidenced that IDO1 knockout greatly downregulated TGF-β-induced expression of pro-fibrogenic factors (*Col1a1*, *Vim*, *ACTA2*) and upregulated gene expressions of *Cdh1* (Fig. 6J). IDO1 knockout dramatically increased TGF-β-induced gene expressions of regulators of mitochondrial fusion (*Opa1, Mfn1, Mfn2*) and inhibited gene expressions of fission (*Dnm1l*) (Fig. 6K). In the meantime, we evaluated mitochondrial function with JC-1. Our data showed that TGF-β significantly induced MLFs' MMP collapse and these changes were markedly exacerbated by the Kyn treatment. Next, we also assessed the potential of the mitochondrial membrane *in vivo* using Mito-Tracker. We observed that TGF-β stimulation caused mitochondrial fission and fragmentation; However, this effect was exacerbated by Kyn treatment for 24 h. (Supporting Information Fig. S8A and S8B).

3.6. IDO1-deletion significantly improved lipid metabolism in PF mice

We sought to discover the roles played by IDO1 in regulating lipid metabolism. The functional enrichment analyses of these shared genes revealed that oxidative phosphorylation, PPAR signaling pathway, and purine metabolism were the predominant metabolic processes impacted in WT and *Ido1* KO mice following BLM treatment. We found several genes participate in lipid metabolism extensively upregulated in *Ido1* KO mice associated with the synthesis of fatty acids, transport of long-chain fatty acids, activation of fatty acids, elongation, and modification (Fig. 7A). Examining genes involved in the biosynthesis of carbohydrate derivatives and the metabolism of nucleoside triphosphates, we observed differential regulation of genes linked to oxidative respiratory complexes and purine metabolism (Fig. 7B).

Next, we investigated how lipogenic genes (PPARγ, PPARγ2, and FASN) affect fibrotic lesions in human and mouse lungs. Immunohistochemistry revealed that PPARγ and PPARγ2 expression was found to be reduced IPF lungs compared to those normal histology controls (Supporting Information Fig. S9A). We also observed that the protein expression of FASN was downregulated in WT mice compared with the lungs of BLM-treated mice, whereas it was increased in BLM-treated *Ido1* KO mice (Fig. S9B and S9C). We then analyzed the fatty acid composition in the lung through imaging mass spectrometry, with a specific emphasis on predominant fatty acids in *Ido1* KO mice. In lung tissues from BLM-treated mice, there was a significant accumulation of unsaturated fatty acids, specifically palmitoleic acid and oleic acid, while saturated fatty acids, such as palmitic acid and stearic acid, were found at minimal levels. The levels of fatty acids examined exhibited a notable elevation in the lungs of BLM-treated *Ido1* KO mice as opposed to BLM-treated mice (Fig. S9D). The study also verified a significant increase in choline, phosphatidylcholine, and PE (P-18:0/22:6) levels in the lungs of BLM-treated *Ido1* KO mice compared with the lung of BLM-treated mice (Fig. S9E). Functional enrichment analyses comparing mBLM-treated WT and *Ido1* KO mice indicated that the deletion of IDO1 significantly impacted the nucleoside phosphate metabolic process in fibrotic lungs, with purine metabolism being the predominant biological pathway encompassed within this annotation. In contrast to BLM-treated mice, IDO1-deletion in mice increased fusion proteins OPA1 levels and thus enhancing mitochondrial fusion-enhanced potentially the capacity for fatty acid oxidation (Fig. S9F), along with activation of *de novo* glycolytic serine/glycine synthesis pathways and mitochondrial one-carbon metabolism (Fig. 7C and D).

3.7. IDO1 is a direct cellular target of WEL in the regulation of mitochondrial dynamics

We performed an in-depth *in silico* high-throughput screening of a small-molecule drug library to evaluate their binding affinity to the significant pocket on IDO1. Notably, the selected library comprised FDA-approved compounds, validated through cytotoxicity evaluations and ready for therapeutic repurposing. After that, each compound was docked into the IDO1 binding site and ranked based on its docking scores (Supporting Information Fig. S10A). Through virtual screening; we obtained a number of valuable antifibrotic agents. Supporting Information Table S3 lists the top 20 drugs with the docking score. Among them, WEL, a small molecule inhibitor of IKK and IKK-related kinases, had the highest docking score with the IDO1 protein. Next, to confirm the direct cellular target of WEL, we employed a small-molecule affinity reagent to capture its binding proteins. We used the IDO1 antibody for Western blot validation (Fig. 8A and B). At the same time, the immunofluorescent colocalization analysis revealed a direct interaction between WEL and IDO1 (Fig. 8C), which was supported by DARTS and CETSA results (Fig. 8D and E).

To confirm that WEL-suppressed fibroblast proliferation was true *via* targeting IDO1. the MLFs were isolated from *Ido1*$^{+/+}$ or *Ido1*$^{-/-}$ mice. IDO1 knockdown and control MLFs were subjected to varying concentrations of WEL, followed by an assessment of cell viability using the CCK8 assay. We found that IDO1 knockdown MLFs did not respond or were very insensitive to the treatment of WEL, suggesting that the antifibrotic activity of WEL is indeed through targeting IDO1 (Fig. 8F). In addition, IDO1 knockdown MLFs were treated with different concentrations of IDO1 inhibitors (1 MT, epacadostat, and navoximod). We found that IDO1 knockdown MLFs showed almost no responsiveness to IDO1 inhibitors (Fig. 8G).

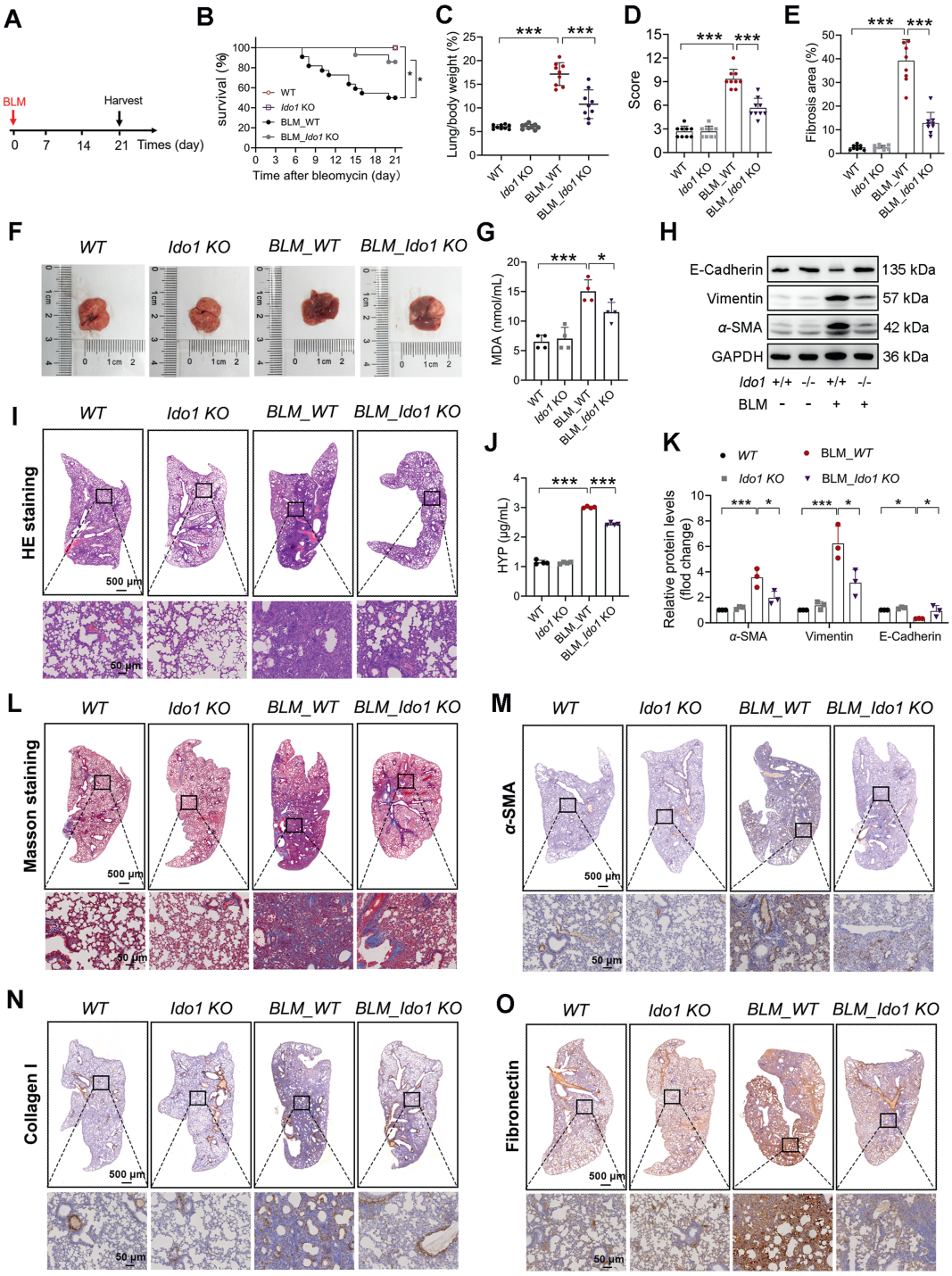

Figure 3 Deletion of IDO1 alleviates BLM-induced lung fibrosis in mice. (A) Scheme of the experimental approach. Mice were sacrificed on Day 21 post-initial BLM exposure. (B) The mortality of mice in each group. $n = 9$ mice per group. (C) The ratio of lung weight to body weight. $n = 9$ mice per group. (D) Statistical analysis of lung injury score. $n = 9$ mice per group. (E) Lung fibrotic score analysis of the lung sections. $n = 9$ mice per group. (F) The gross appearance of lungs (Scale bar, 1 mm). $n = 6$ mice per group. (G, J) ELISA measured serum MDA (G) and HYP (J) contents. $n = 4$ samples per group. (H, K) Western blots (H) and quantitative results (K) of E-Cadherin, Vimentin, α-SMA in lungs from WT and *Ido1* KO mice 21 days post initial BLM exposure. $n = 3$ mice per group. (I, L) Hematoxylin & eosin (I), and Masson's trichrome staining (L) from WT and *Ido1* KO mice 21 days after BLM. Scale bar, 50 μm. $n = 6$ mice per group. (M−O) Images of immunohistochemical staining using indicated antibodies. Scale bars, 50 μm. $n = 6$ mice per group. All data are presented as mean ± SD, one-way ANOVA with Turkey's multiple-comparison test, $^*P < 0.05$, $^{**}P < 0.01$, $^{***}P < 0.001$.

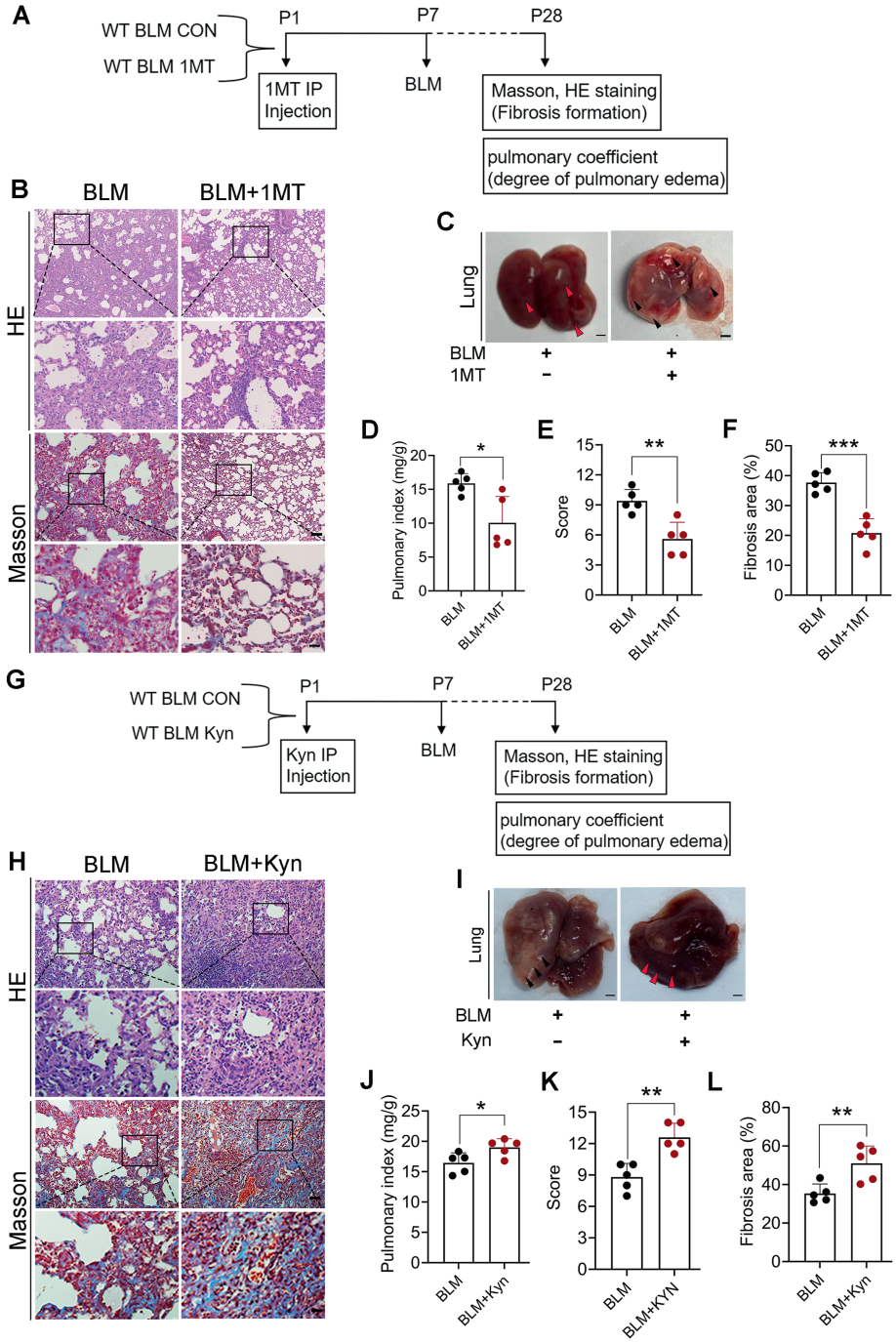

Figure 4 The effects of Kyn on pulmonary fibrosis. (A) Flowchart of the *in vivo* experiments. WT mice were intraperitoneally injected with 1 MT (100 mg/kg) or saline (Control, Ctrl) every other day from P1 up to P28 and underwent a single injection of BLM at P7. (B−F) The gross appearance of histological changes (B, D, E), lung fibrosis (B, F) and whole lungs (C) were observed and analyzed at P28. $n = 5$ mice per group. (G) Flowchart of the *in vivo* experiments. WT mice were intraperitoneally injected with Kyn (20 mg/kg) or saline (Control, Ctrl) every other day from P1 up to P28 and underwent a single injection of BLM at P7. (H−L) The gross appearance of histological changes (H, J, K), lung fibrosis (H, L) and whole lungs (I) was observed and analyzed at P28. $n = 5$ mice per group. All data are presented as mean ± SD, one-way ANOVA with Turkey's multiple-comparison test, $^{*}P < 0.05$, $^{**}P < 0.01$, $^{***}P < 0.001$.

In order to investigate the WEL-binding sites on IDO1, molecular dynamics simulations were conducted. Root mean square deviation (RMSD) for the WEL−IDO1 complex kept around 2 Å (Fig. 8H) and showed binding energies of −9.118 kcal/mol during the 100 ns molecular dynamics simulations, indicating the WEL-IDO1 complex Stability (Fig. S10B−S8D). In the RMSF plot, the observed WEL was bound to IDO1 formed a rigid structure during MD simulation (Fig. 8I). There were still about 1−4 hydrogen

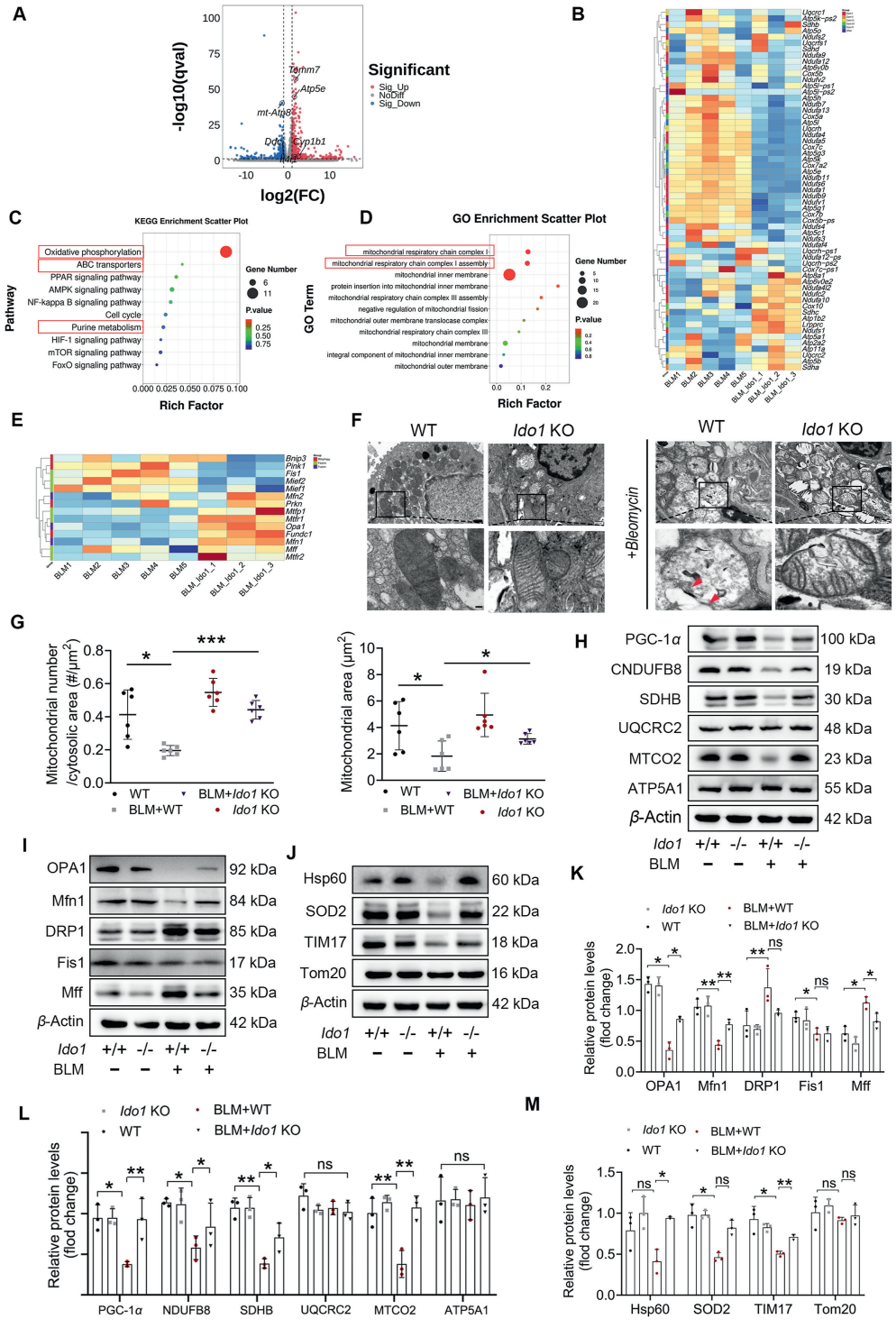

Figure 5 Genetic knockout of IDO1 restores mitochondrial dynamics and bioenergetics in a murine lung fibrosis model. (A) Differentially expressed genes between mBLM-treated WT mice and *Ido1* KO mice were determined by RNA-Seq and shown by volcano plot. (B) Heatmap showing differentially expressed mitochondrial respiratory electron transport chain (ETC, complexes I−V) genes in mBLM-treated WT and *Ido1* KO mouse lungs. (C, D) The KEGG (C) and GO (D) enrichment analysis of RNA-sequencing data. (E) Heatmap showing differentially expressed mitochondrial dynamics-associated genes in mBLM-treated WT and *Ido1* KO mouse lungs (BLM-treated mice, WT: $n = 5$, KO: $n = 3$). (F) Representative TEM images show mitochondrial ultrastructural changes in mBLM-treated WT and *Ido1* KO mouse lungs ($n = 3$ mice per group) with disrupted cristae marked with red arrowheads (scale bar, upper row 500 nm, lower row 1000 nm). (G) Quantification of mitochondrial number per μm^2 and mean mitochondrial area. (H, L) Representative blots and quantitative analysis of ETC complex subunits from indicated groups. (I, K) Representative blots and quantitative analysis of mitochondrial fission/fusion-related proteins, including OPA1, Mfn1, DRP1, Fis1, and Mff ($n = 3$). (J, M) Representative blots and quantitative analysis of mitochondrial mass proteins-related proteins including Hsp60, SOD2, TIM17, Tom20 ($n = 3$). All data are presented as mean ± SD, one-way ANOVA with Turkey's multiple-comparison test, $^*P < 0.05$, $^{**}P < 0.01$, $^{***}P < 0.001$, ns = non-significant.

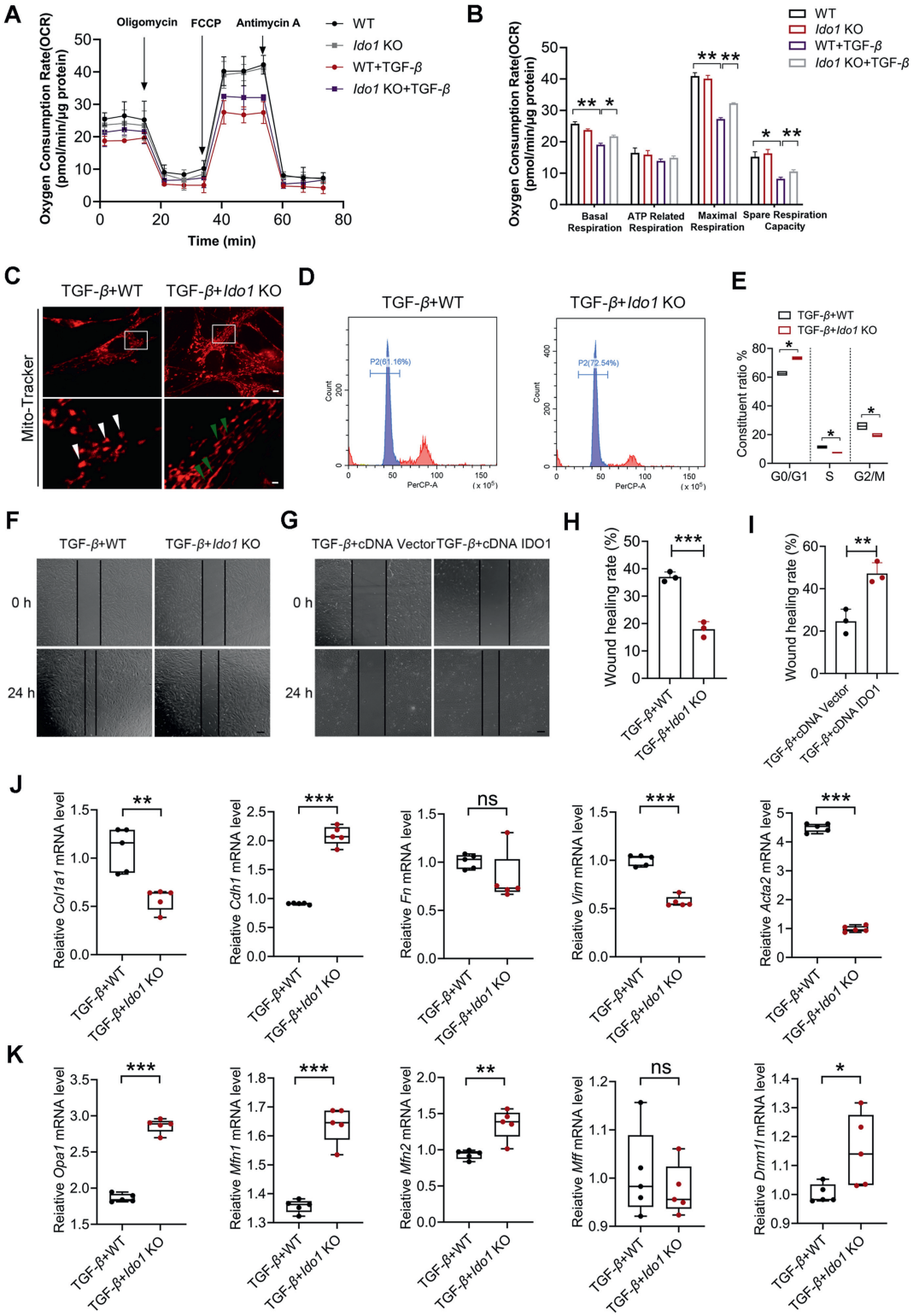

Figure 6 IDO1-deficient pulmonary fibroblasts prevent TGF-β-induced EMT and mitochondrial damage. (A) Representative OCR profile at baseline and after the injection of oligomycin (1 μmol/L), FCCP (1 μmol/L), and rotenone/antimycin (0.5 μmol/L). (B) Quantitative results of basal respiration, ATP-linked respiration, maximal respiration, and spare respiratory capacity. (C) Genetic knockout of IDO1 promoted mitochondrial fusion against TGF-β-induced mitochondrial damage. Arrows (Green) indicate branched healthy mitochondria. Arrows (white) indicate spherical dysfunctional mitochondria (scale bar: 20 μm). (D) Representative images of cell cycle assay of MLFs from WT and *Ido1* KO mice were treated with 10 ng/mL TGF-β. (E) Representative cell cycle analysis diagram. (F) The MLFs were isolated from WT and *Ido1* KO mice. Scratch assay was used to examine the effect of genetic knockout of IDO1 on TGF-β-induced lung fibroblast migration (scale bar: 20 μm). (G) The Flag-tagged IDO1 overexpression plasmid and the corresponding control plasmid were transfected into HLFs. Scratch assay was used to examine the

bonds between WEL and K242, V378, S239, R235, S245 in the molecular dynamic stimulation (Fig. S10E). We mutated K242, V378, S239, R235, S245 into K242A, V378A, S239A, R235A, S245A, respectively, for exploration of their roles. The K242 and V378 mutations abolished protection against mitochondrial damage of WEL in TGF-β-stimulated MLFs, as well (Fig. S10F). To verify this assumption, we mutated K242 into K242A, V378 into V378A, and K242/V378 into K242A/V378A (double mutation). *In vitro*, pull-down assay indicated that both K242 and K242/V378 mutations greatly decreased the binding ability of WEL for IDO1. Nevertheless, the V378 mutation showed a relatively weaker association, suggesting that K242 was a potential binding site of WEL on IDO1 (Fig. 8J and K). These results demonstrated that WEL is directly bound to IDO1 through 242 lysine. Covalent docking analysis evidenced that WEL binds to IDO1 through the formation of a covalent bond (2 Å) with the K242 residue (Fig. 8L). After that, to verify the fundamental biological roles of K242, we transfected IDO1 and IDO1 (K242A) plasmids into primary cultured *Ido1* KO mouse lung fibroblasts. We found that the cytoprotective effect induced by WEL was significantly reversed upon reintroducing IDO1, but not with its mutant variant, IDO1 (K242A) (Fig. 8M), suggesting that the K242 residue on IDO1 is crucial for WEL's binding and subsequent anti-fibrotic outcomes.

3.8. IDO1 inhibitors effectively alleviate the differentiation of the lung fibroblasts

Mouse lung cells underwent treatment with different doses of WEL for 48 h. Results showed that 10, 20, and 40 μmol/L of WEL significantly reduced cell viability, while 1.25, 2.5, and 5 μmol/L were considered safe concentrations (Fig. 9A and B). Moreover, compared to the TGF-β-mediated-MLFs, treatment with WEL (1.25, 2.5, and 5 μmol/L) significantly reduced protein levels of conventional fibroblast markers, including α-SMA and Vimentin (Fig. 9D). Next, we determined the mitochondrial membrane potential. Our data showed that TGF-β significantly induced HLFs' MMP collapse and these changes were greatly weakened by WEL administration (Fig. 9C). TGF-β caused remarkable mitochondrial fragmentation; Nevertheless, this situation was alleviated by WEL administration, both in MLFs (Fig. 9E) and in HLFs (Fig. 9F). Moreover, TGF-β induced MLFs exhibited suppressed mitochondrial respiratory capacities including basal respiration, ATP-linked respiration, maximal respiration, and spare respiratory capacity. Treatment with WEL remarkably increased basal respiration, ATP-linked respiration, maximal respiration, and spare respiratory capacity (Fig. 9G and H). Because WEL significantly reduced protein levels of conventional fibroblast markers, we therefore seek to uncover WEL's effect on cell proliferation. The findings indicate that G0/G1 phase of TGF-β group is significantly reduced while S and G2/M phases are elevated comparing to the control group. WEL (5 μmol/L) significantly reduced S and G2/M phases proportion, both in MLFs (Fig. 9I and J) and in HLFs (Supporting Information Fig. S11A and S11B).

3.9. Targeting IDO1 by Wedelolactone effectively suppressed the progression of PF

Next, we studied the protective effects of WEL on lung injury in mouse models (Fig. 10A, Supporting Information Fig. S12A), and compared its effects with the antifibrotic medication nintedanib. HE and Masson staining data suggested that WEL significantly attenuated sBLM and mBLM-induced lung injury and fibrosis (Fig. 10B−D, Fig. S12B−S12D). WEL significantly decreased pulmonary edema (Fig. 10E, Fig. S12E) and reduced HYP and MDA in serum (Fig. 10F and G). In the sBLM-induced PF model, WEL improved the body weights of mice (Fig. 10H), which was, however, no change in the mBLM-induced PF model (Fig. S12F). WEL treatment markedly inhibited IDO1 (Fig. 10I and J), and α-SMA expression (Fig. 10K and O, Fig. S12G and S12H). WEL also enhanced E-cadherin expression and suppressed Vimentin expression (Fig. 10K and O) and collage deposition (Fig. S12G and S12I). Consistent with these data, the expression of ETC complex protein (Fig. 10L and P) and mitochondrial fusion proteins (OPA1, Mfn1, Mfn2, Mff) (Fig. 10M, N, Q, R) were upregulated by WEL. In comparison with WEL (20 mg/kg), nintedanib at the concentration (40 mg/kg) displayed similar effects on lung injury, fibrosis (Fig. 10B−D, Fig. S12B−S12D), pulmonary edema (Fig. 10E, Fig. S12E), the serum level of HYP and MDA (Fig. 10F and G), and some markers such as α-SMA, Vinmentin, and E-cadherin expression (Fig. 10K and O).

In the mBLM-induced lung fibrosis model, we observed a significant upregulation of common genes in mice treated with both nintedanib and WEL (Supporting Information Fig. S13A and S13B). The KEGG and GO enrichment analysis determined ECM−receptor interaction, oxidative phosphorylation, and mitochondrial inner membrane as primary metabolic processes effected in mice treated with nintedanib and WEL after BLM treatment (Fig. S13C−S13F). Examination of metabolites included in the tricarboxylic acid (TCA) cycle and nucleotide metabolism, we found downregulation of metabolites involving ATP, ADP, GMP, and citric acid in fibrotic lungs of mice. Treated with nintedanib and WEL increased mitochondrial ATP, ADP, GMP production, and the content of citric acid. As can be seen, treated with WEL achieves significantly better regulation than nintedanib (Fig. S13G and S13H).

To investigate whether IDO1 mediates the lung protective properties of WEL, we used an *Ido1* KO mouse model (Fig. 11A). Administration of WEL (20 mg/kg) failure to decrease lung injury and lung fibrosis further following exposure to BLM, as indicated by HE and Masson staining in *Ido1* KO mice (Fig. 11B and C). In line with this, WEL has no further inhibitory effect on BLM-induced α-SMA expression (Fig. 11B and D), fibronectin elevation (Fig. 11B and E), and collage production (Fig. 11B and F) in *Ido1* KO mice. WEL did not significantly alter mitochondrial morphology and mitochondrial numbers in *Ido1* KO mice (Supporting Information Fig. S14A). In addition, the mitochondrial dynamics genes (*Opa1, Mfn1, Mfn2, Dnm1l*) (Fig. 11G) and FASN expression (Fig. S14B) were not further improved by WEL

effect of IDO1 overexpression on TGF-β-induced human lung fibroblast migration (scale bar: 20 μm). (H) Quantitative analysis of the scratch wound area of MLFs from WT and *Ido1* KO mice. (I) Quantitative analysis of the IDO1 overexpression plasmid's scratch wound area was transfected into HLFs. (J) Relative *Col1a1*, *Cdh1*, *Fn*, *Vim*, *Acta2* mRNA levels in MLFs from WT and *Ido1* KO mice were treated with 10 ng/mL TGF-β. (K) Relative *Opa1*, *Mfn1*, *Mfn2*, *Mff*, and *Dnm1l* mRNA levels in MLFs from WT and *Ido1* KO mice were treated with 10 ng/mL TGF-β. All data are presented as mean ± SD ($n = 3$), one-way ANOVA with Turkey's multiple-comparison test, $^{*}P < 0.05$, $^{**}P < 0.01$, $^{***}P < 0.001$, ns = non-significant.

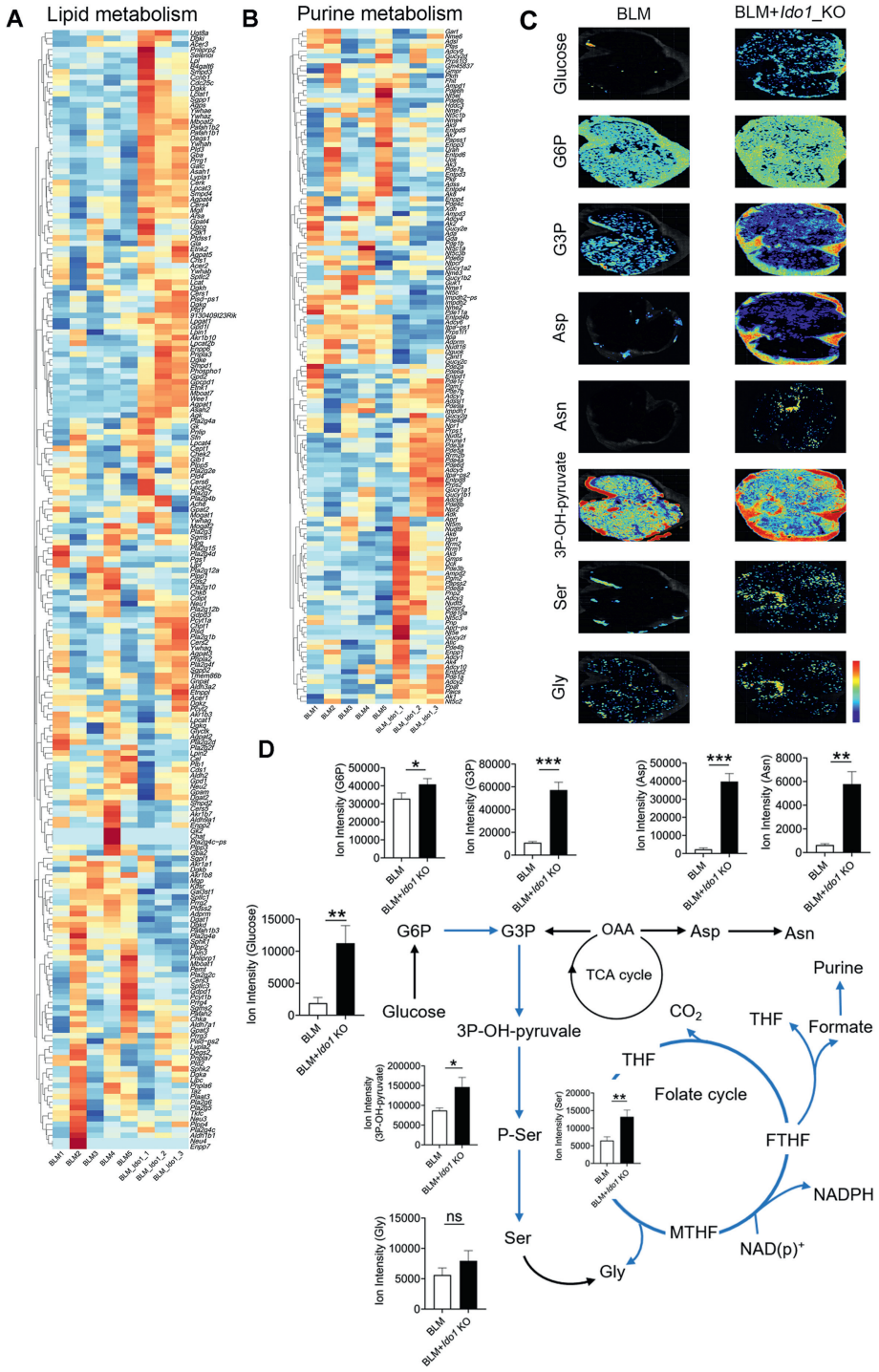

Figure 7 Genetic knockout of IDO1 upregulates lipid metabolism in a murine lung fibrosis model. (A, B) Heatmaps to show genes related to lipid metabolism under the annotation fatty acid metabolic process (A) and genes related to purine metabolism under the annotation purine ribonucleoside triphosphate metabolic process (B) (BLM-treated mice, WT: $n = 5$, KO: $n = 3$). (C, D) MALDI-MSI of metabolites involved in glycolysis, asparagine (Asn) synthesis, *de novo* serine/glycine synthesis, and mitochondrial one-carbon metabolism in the lungs (Glucose; G6P, glucose-6-phosphate; G3P, glyceraldehyde-3-phosphate; Asp, aspartate; Asn, asparagine; 3P−OH-pyruvate, 3-phosphohydropyruvate; Ser, serine; Gly, glycine), ($n = 3$). All data are presented as mean SD, one-way ANOVAwith Turkey's multiple-comparison test, $^{*}P < 0.05$, $^{**}P < 0.01$, $^{***}P < 0.001$, ns = non-significant.

treatment in *Ido1* KO mice. Subsequently, we also discovered that treatment of WEL (20 mg/kg) failed to reduce further the expression of key enzymes implicated in KP in *Ido1* KO mice (Supporting Information Fig. S15A−S15E).

4. Discussion

IPF is a rapidly progressing and often fatal lung disease marked by the abnormal buildup of myofibroblasts, which secrete ECM,

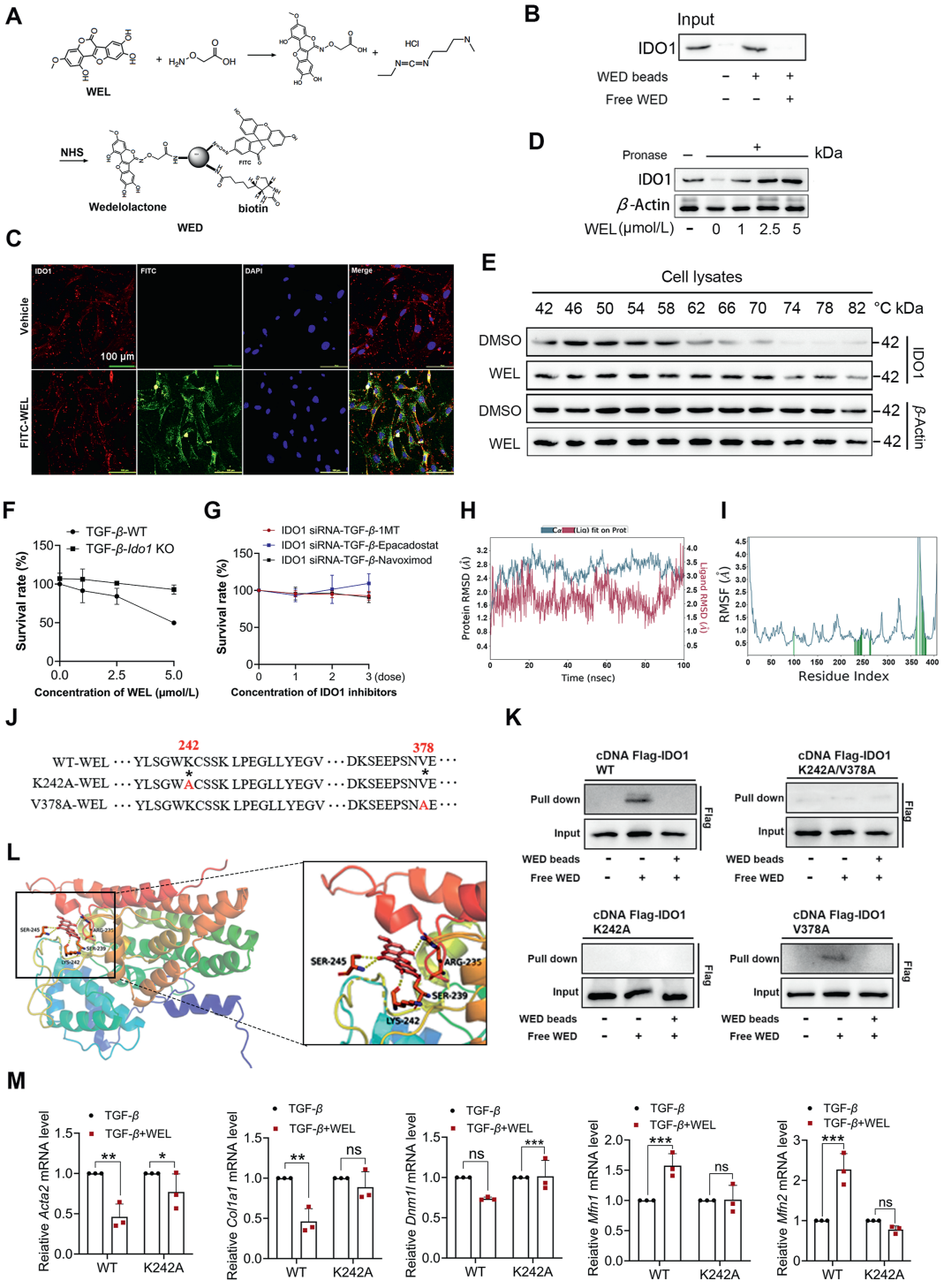

Figure 8 IDO1 is a direct cellular target of WEL. (A) The scheme of BSA-Wedelolactone-FITC-Biotin complex (WED). (B) WEL selectively bound to IDO1 by pull-down analysis ($n = 3$). (C) The colocation of WED with IDO1 detected by the fluorescence microscope ($n = 3$). (D) WEL promoted IDO1 resistant to proteases by DARTS analysis ($n = 3$). (E) WEL promoted IDO1 resistance to different temperature gradients by CETSA analysis. (F) CCK8 assay for the viability of control and *Ido1*-knockdown MLFs treated with WEL ($n = 3$). (G) CCK8 assay for the viability of *Ido1*-knockdown MLFs treated with Ido1 inhibitors in clinical or preclinical trials ($n = 3$). (1 MT, dose 1: 25 μmol/L, dose 2: 50 μmol/L, dose 3: 100 μmol/L; Epacadostat, dose 1: 20 nmol/L, dose 2: 50 nmol/L, dose 3: 100 nmol/L; Navoximod, dose 1: 100 nmol/L, dose 2: 250 nmol/L, dose 3: 500 nmol/L). (H) The RMSD plot analyzed by molecular dynamics. (I) The RMSF plot analyzed by molecular dynamics. (J, K) IDO1 (K242A), but not IDO1 (V378A), is responsible for WEL binding to IDO1. Mouse primary lung fibroblasts were transfected with Flag-tagged IDO1 and its mutant plasmids. The Lys and Val labeled by * were potential modification sites. (L) Docking analysis of WEL covalent binding mode to IDO1. (M) K242A mutations abolished the mitochondrial damage of WEL in TGF-β-stimulated mouse primary lung fibroblasts ($n = 3$). All data are presented as mean ± SD, one-way ANOVA with Turkey's multiple-comparison test, $^*P < 0.05$, $^{**}P < 0.01$, $^{***}P < 0.001$, ns = non-significant.

leading to fibrosis and deterioration of lung structure, respiratory insufficiency, and ultimately, mortality[37-39]. We summarized our study's findings here, including: (I) Our findings reveal a significant upregulation of IDO1 in the lungs of both IPF patients and mice injured by BLM, showing a positive correlation with genes characteristic of fibrosis; (II) We identified IDO1 as a promoter of lung fibrosis through the use of IDO1 knockout mice and lung fibroblast models; (III) Mechanistically, IDO1-deletion activated profound mitochondrial fusion-enhanced potentially the capacity for fatty acid oxidation, accompanied by activation of *de novo* glycolytic serine/glycine synthesis pathways and mitochondrial one-carbon metabolism; (IV) WEL, a small molecule IKK inhibitor screened from the Natural Product Library, displayed a high affinity to IDO1 and significantly attenuated lung fibrosis. In conclusion, IDO1 plays a critical role in initiating and progressing PF, suggesting that approaches focused on inhibiting or reducing IDO1 expression may offer viable therapeutic strategies for treating this condition.

Research on the association between PF and KP has mainly concentrated on Trp[40,41], and the relationship between the metabolite level of Trp and PF has yet to be studied. Significantly, there was a notable correlation between the metabolite levels of Trp and the pathologic grade of PF. These results show that the accumulation of Trp metabolites may significantly influence the development of PF. IDO1 is the first and rate-limiting enzyme of Trp catabolism and has essential roles in many pathophysiological processes. Moreover, its function in the pathologic progression of PF warrants further exploration.

IDO1 is a high context-dependence enzyme with two essential roles in biological processes: the provider of one carbon unit and immunosuppression[42]. Trp degradation along the Kyn pathway is an anti-ROS redox reaction. IDO1 itself is closely associated with the ROS levels, as generating and clearance ROS was reported to mediate IDO1 expression upregulation or downregulation in dendritic cells[43]. IDO1 catalytic activity-based ROS clearance sustains myeloid-derived suppressor cell mediators and represents a critical mechanism mediating immune suppression in the myeloid IDO1[44]. In addition, the canonical proteins associated with mitochondrial dynamics and mitophagy exhibited significant alterations in macrophages lacking IDO1 and were treated with 1 MT[45]. Here, we found that IDO1 protein levels are significantly upregulated in the lungs of IPF patients and BLM-induced PF in mice. Our research indicates that IDO1 directly induces pulmonary dysfunction and fibrosis by destroying mitochondrial bioenergetics. As IDO1 is known to regulate multiple genes playing roles in mitochondrial dynamics simultaneously, we discovered that Mfn1/2 targets are regulated by IDO1 inhibition. We chose to focus on this regulatory axis because of the widely demonstrated relevance of Mfn1/2 to mitochondrial dysregulation, which is observed in our study, and because of the potential significance of establishing fibrosis-associated Mfn1/2-activation mechanisms in cells within lung tissue[46]. It has been previously shown that mitochondrial dysfunction induces EMT through TGF-β/Smad/Snail signaling *via* c-Jun/AP-1 activation[47]. Smad2 is a critical determinant of mitochondrial dynamics. Mfn2 and Rab and Ras Interactor 1 as new Smad2 binding partners required for mitochondrial fusion[48]. TGF-β3 activated canonical p-Smad3 signaling and resultantly mediated AMPK-induced mitochondrial fission[49]. Thus, we suggest that Mfn1/2 expression is downregulated by IDO1 during oxidative stress, disturbing the balance of mitochondrial dynamics, promoted mitophagy, activated inflammation, as well as TGF-β/Smad signaling pathway may be the underlying mechanism by which IDO1 contributes to fibrogenesis. Still, the underlying mechanisms of IDO1 affect the TGF-β signaling pathway by influencing mitochondrial function, which needs further investigation.

Here, we reveal critical functions for IDO1 in mitochondrial bioenergetics, fatty acids and lipid metabolism, and PF development. Previous reports have demonstrated that *Ido1* gene knockout reduced the excessive accumulation of lipids in TAA-treated liver[50]. Mitochondrial fusion and lipid metabolism correlate well with modulating AEC2 cell damage and subsequent fibrotic remodeling[46]. In our study, we demonstrated a direct connection between IDO1 and mitochondrial function, dynamics, and lipid metabolism, providing substantial support for our working hypothesis. This was further supported by the transcriptome analysis of *Ido1* KO mice, which showed that loss of IDO1-activated profound mitochondrial fusion potentially enhanced the capacity for fatty acid oxidation.

Obtaining insights into the role of the rate-limiting enzyme IDO1 in regulating lipid metabolism within IPF and healthy lung tissues presents significant technical challenges. In the present report, we provide evidence that IDO1 regulates lipid metabolism in the mouse lung tissue, which significantly influences surfactant lipid production in these histiocytes and is essential for the development of PF. However, this study confirms mitochondrial fragmentation and activation of *de novo* glycolytic serine/glycine synthesis pathways and mitochondrial one-carbon metabolism in response to BLM-induced mitochondrial damage. It is hypothesized that histiocytes increase the expression of lipids in response to mitochondrial damage to sustain surfactant lipid synthesis in the presence of histiocyte injury. The disruption of surfactant integrity results in the impairment of typical lung function and may contribute to the progression of PF[51-53]. Our findings suggest that IDO1 deficiency enhances fatty acid oxidation in lung tissue following BLM-induced mitochondrial damage. Furthermore, we provide evidence that enhanced regulation of lipid metabolism in *Ido1* KO mice mitigates lung fibrosis. These results align with previous research indicating that IDO1 exacerbates Acetaminophen-induced acute liver failure by promoting excessive lipid peroxidation[54] and that improves liver fibrosis in zebrafish by IDO1 knockout to the regulation of lipid metabolism[50]. Our findings also align with IDO1 directly regulating the interaction between mitochondrial dysfunction and lipid metabolism[55,56]. To pursue additional clinical evidence for our hypothesis, we assessed 5 patients with PF and 5 healthy control patients. PPARα regulates gene expression in fatty acid β-oxidation and energy homeostasis[57-59]. Impairment of the pathway for fatty acid oxidation and PPARα exacerbates fibrosis during aging[59]. At present, it remains unclear whether the modifications noted in PPARα in patients with PF reflect abnormalities of tissue function. Nevertheless, we showed that in patients with PF and healthy control patients, there was a correlation between PPARα and fatty acid oxidation.

The development of candidate drugs for interaction with IDO1 molecules remains a challenge. We employed a high-throughput *in silico* screen to identify IDO1 interacting compounds from small molecule drugs. WEL, a small molecule IKK inhibitor, reflected a stronger binding affinity with IDO1 compared with other compounds. WEL suppressed IDO1 enzyme activity and protein expression, promoting mitochondria energy metabolism and sustaining mitochondrial function. Consistent with the results of the affinity assay, WEL demonstrated notable lung-protective properties in the BLM-induced mouse model. Compared with WEL

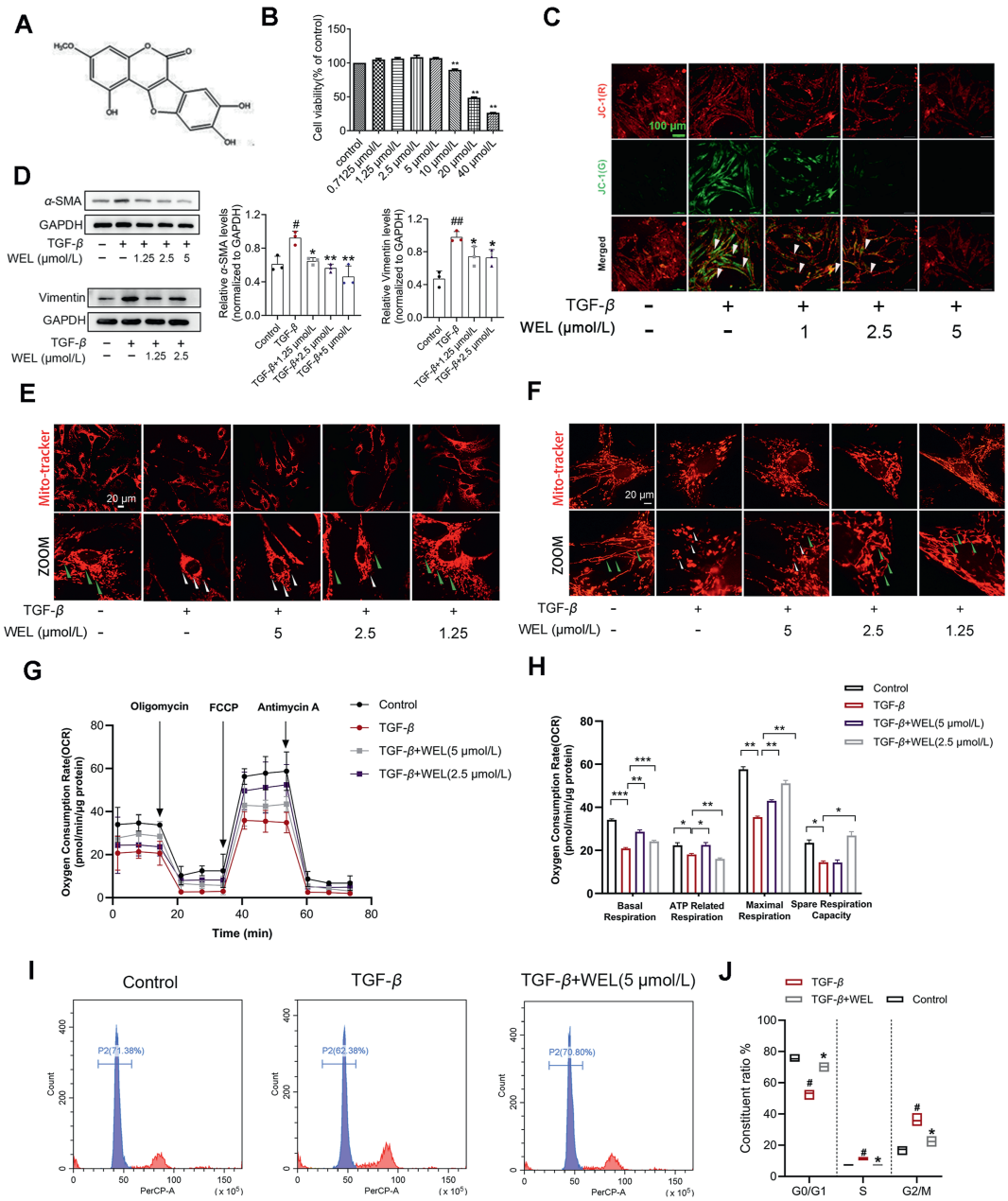

Figure 9 WEL attenuates TGF-β-mediated EMT and mitochondrial damage *in vitro*. (A) Chemical structure of WEL. (B) A colorimetric CCK8 assay was performed to measure the cytotoxicity of WEL at various concentrations in cultured MLFs ($n = 5$). (C) WEL blocked TGF-β-induced decrease in mitochondrial membrane potential (MMP) in HLFs, which was detected by JC-1 staining. Arrows indicate depolarized mitochondria (scale bar: 100 μm) ($n = 5$). (D) WEL (1.25, 2.5, and 5 μmol/L) decreased α-SMA, vimentin protein expression, which was analyzed by Western blot ($n = 3$). (E) WEL promoted mitochondrial fusion against TGF-β insult in MLFs. Arrows (green) indicate branched healthy mitochondria. Arrows (white) indicate spherical dysfunctional mitochondria (scale bar: 20 μm) ($n = 3$). (F) WEL promoted mitochondrial fusion against TGF-β insult in HLFs. Arrows (green) indicate branched healthy mitochondria. Arrows (white) indicate spherical dysfunctional mitochondria (scale bar: 20 μm) ($n = 3$). (G) Representative OCR profile at baseline and after the injection of oligomycin (1 μmol/L), FCCP (1 μmol/L), and rotenone/antimycin (0.5 μmol/L). (H) Quantitative results of basal respiration, ATP-linked respiration, maximal respiration, and spare respiratory capacity ($n = 3$). (I) Representative images of cell cycle assay of 24 h WEL treatment on MLFs. (J) Representative cell cycle analysis diagram ($n = 3$). Data are expressed as the mean ± SD. $^{\#}P < 0.05$, $^{\#\#}P < 0.01$ *vs*. control group, $^{*}P < 0.05$, $^{**}P < 0.01$ *vs*. TGF-β group.

(20 mg/kg), nintedanib at the concentration (40 mg/kg) demonstrated effects similar to those on lung injury and fibrosis. Several reports have also demonstrated that WEL improved lung injury by regulating GSK3β-mediated NF-κB and Nrf2 pathways[60]. Also, WEL is an inhibitor of the IKK[61] which will target many proteins beyond IDO1 and may be involved in other myofibroblast regulatory pathways[62]. Through complex, unique, interconnected signaling pathways, WEL could potentially reduce lung fibrosis. Our evidence indicates that IDO1 directly interacts with WEL, and IDO1 is necessary for this compound's lung protective properties.

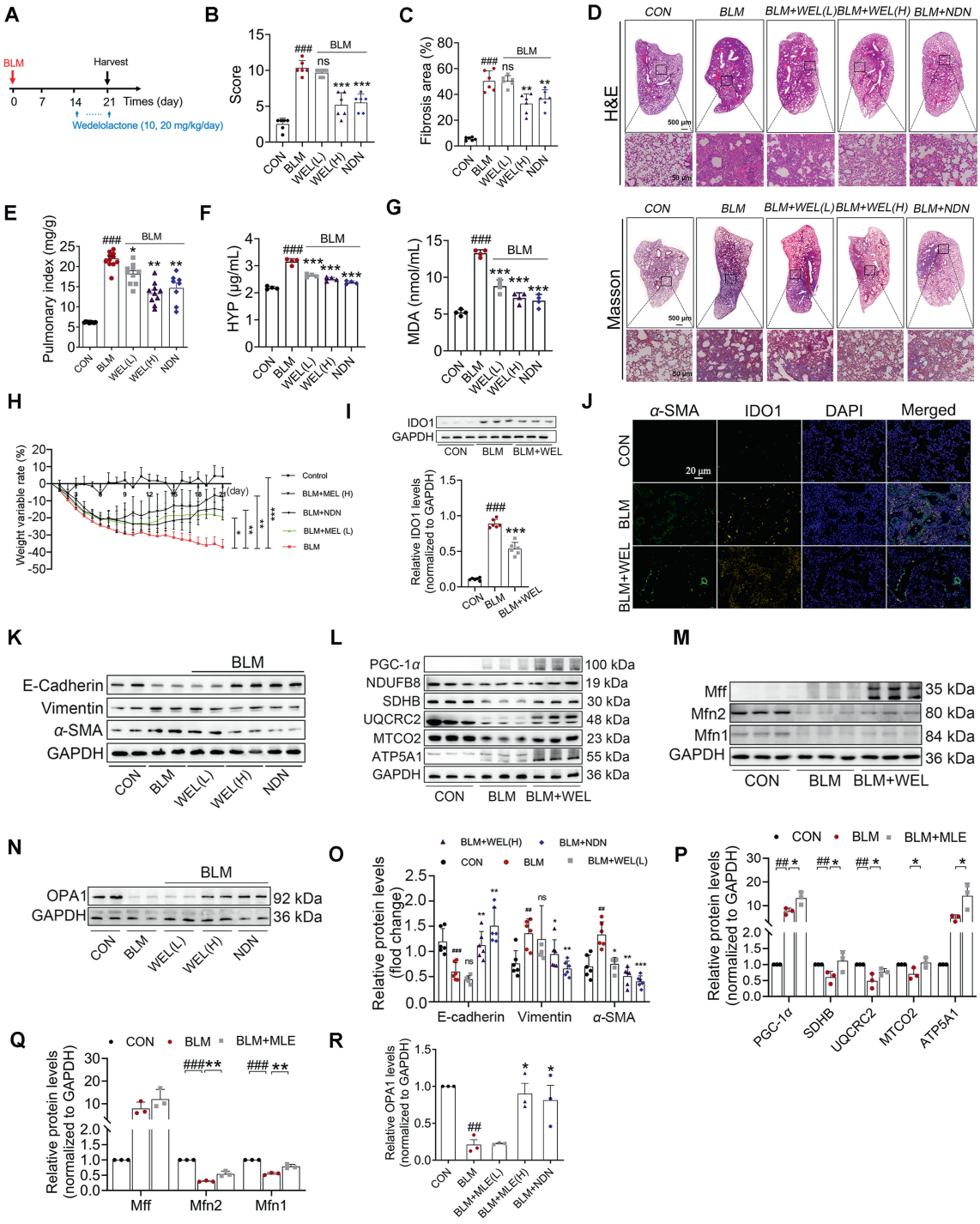

Figure 10 Suppressing IDO1 with WEL alleviates BLM-induced lung fibrosis. (A) Scheme of the experimental approach. Mice were sacrificed on Day 21 post-initial BLM exposure. (B) Statistical analysis of lung injury score. $n = 6$ mice per group. (C) Lung fibrotic score analysis of the lung sections. $n = 6$ mice per group. (D) Hematoxylin, eosin (HE), and Masson's trichrome staining from control (Ctrl) and WEL-treated mice 21 days after BLM. Scale bar, 50 μm. $n = 6$ mice per group. (E) The ratio of lung weight to body weight. $n = 9$ mice per group. (F) Serum HYP contents were measured by ELISA. $n = 4$ samples per group. (G) Serum MDA contents were measured by ELISA. $n = 4$ samples per group. (H) Percent change of mouse body weight. $n = 9$ mice per group. (I) Western blot analysis showing the protein expression levels of IDO1 in each group. $n = 9$ mice per group. (J) Representative images of IDO1 and α-SMA co-immunofluorescence staining in lung tissues. Scale bars = 20 μm. $n = 3$ samples per group. (K, O) Representative blots and quantitative analysis of EMT and extracellular matrix associate gene. $n = 9$ samples per group. (L, P) Representative blots and quantitative analysis of ETC complex subunits from indicated groups. $n = 3$ samples per group. (M, N, Q, R) Representative blots and quantitative analysis of mitochondrial fission/fusion-related proteins, including Mff, Mfn2, Mfn1, and OPA1. $n = 3$ samples per group. Data are expressed as the mean ± SD. $^{\#}P < 0.05$, $^{\#\#}P < 0.01$, $^{\#\#\#}P < 0.001$ *vs.* control group, $^{*}P < 0.05$, $^{**}P < 0.01$, $^{***}P < 0.001$ *vs.* BLM group.

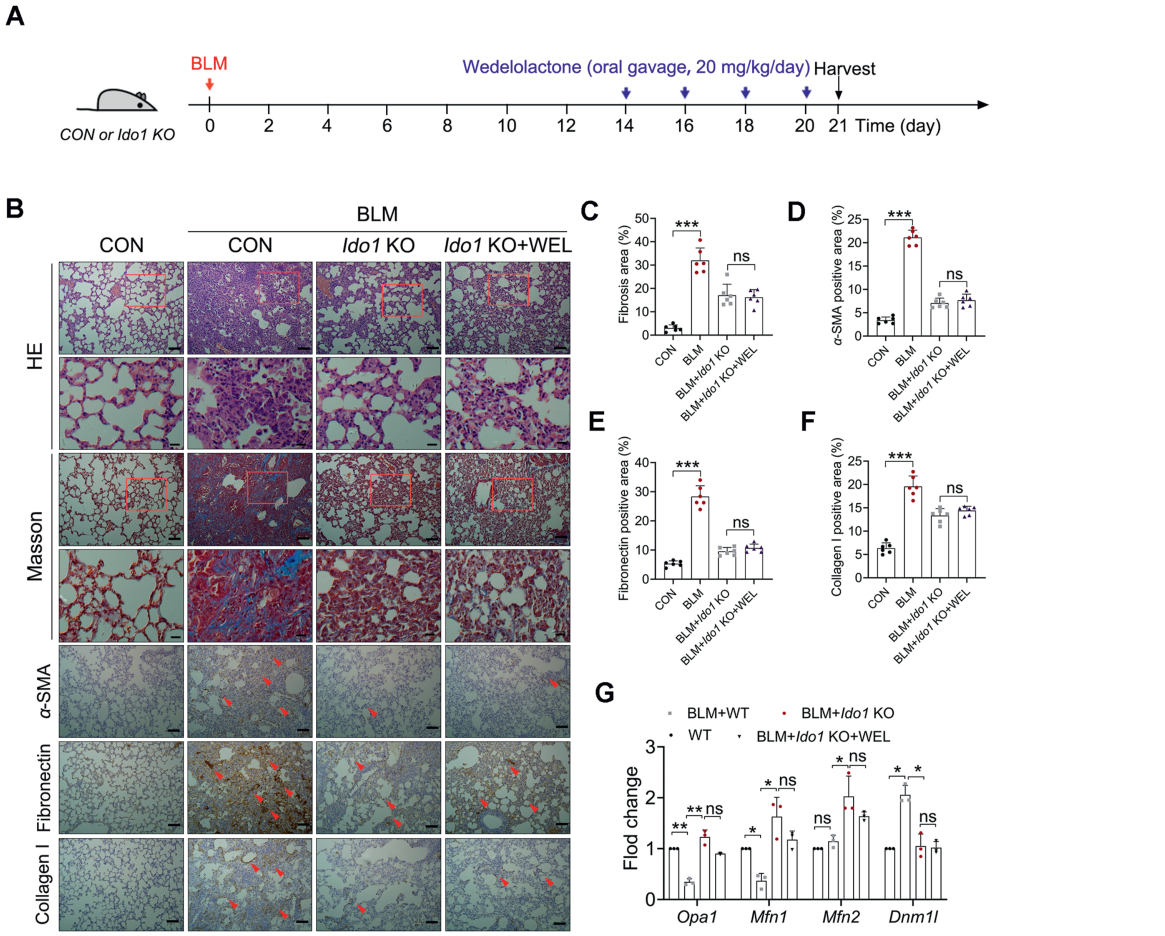

Figure 11 IDO1 mediates the lung-protective effects of WEL. (A) Scheme of the experimental approach. *Ido1* KO mice were treated with WEL at the indicated doses for 7 consecutive days starting on Day 14 post-initial BLM exposure. (B) Lung cross-sections stained with HE (Scale bar, 50 μm), Masson's trichrome (Scale bar, 50 μm), immunohistochemical staining with α-SMA, Fibronectin, and Collagen I (Scale bar, 50 μm). $n = 6$ mice per group. The red arrow indicates a positive area. (C) Statistical results for interstitial collagen in (B) were analyzed using Image Pro-Plus software. $n = 6$ mice per group. (D−F) Quantification of staining of α-SMA (D), Fibronectin (E), and Collagen I (F). $n = 6$ mice per group. (G) mRNA levels of the indicated genes in lungs determined by qRT-PCR. $n = 3$ mice per group. Gene expression levels were normalized to GAPDH. All data are presented as mean ± SD, one-way ANOVA with Turkey's multiple-comparison test, $^*P < 0.05$, $^{**}P < 0.01$, $^{***}P < 0.001$, ns = non-significant.

The currently available small-molecule regulators that target the IDO1 family bind to the catalytic pocket of IDO1[63]. Here, we identified an unexpected pharmacological binding domain featuring a K242 covalent site at a considerable distance from the known catalytic pocket. The three-dimensional configuration of the IDO1 subunit bound with WEL displayed a distinct ligand-binding pocket, which contained V378, S239, R235, and S245 residues; this pocket offers a molecular foundation for the formation of hydrogen bonds between WEL and IDO1. Additionally, the formation of hydrogen bonds may serve as a critical prerequisite for enhancing the covalent linkage of WEL at the K242. Therefore, the ligand-binding pocket likely encompasses a variety of intermolecular forces and facilitates the discovery of novel small-molecule regulators for IDO1. Moreover, we investigated the likelihood of off-target effects of WEL against IDO1 targets. Data suggested IDO1 knockdown MLFs did not respond or were insensitive to treating WEL. To exclude the possibility of WEL off-target effects, we tested additional IDO1 inhibitors. The comparable effects elicited by three small-molecule IDO1 inhibitors with distinct molecular structures provide evidence against off-target effects.

A previous study has shown that inhibition of IDO1 can increase immune response and might predispose patients to an increased risk of respiratory infections, including pneumonia[64], raising concerns for the potential pharmaceutical application of IDO1 inhibitors. Inhibition of IDO1 activity has been shown to be effective in treating fibrosing disorders[24], including pulmonary fibrosis. IDO1 inhibition was demonstrated to have an anti-fibrotic effect by recruiting immune cells[24], which, in turn, are known to secrete proinflammatory soluble factors such as IL-6 and IFN-γ in various target cells, including lung epithelial cells and alveolar macrophages. The expression of IDO1 in patients with pneumonia was tightly linked to a higher host inflammatory response and increased IL-6 gene expression[23,44]. Clinical studies justifying the use of such agents are currently lacking. As PF patients are at increased risk of pneumonia events and IDO1 inhibition has been linked to an increased risk of pneumonia, the potential for an additive risk must be considered.

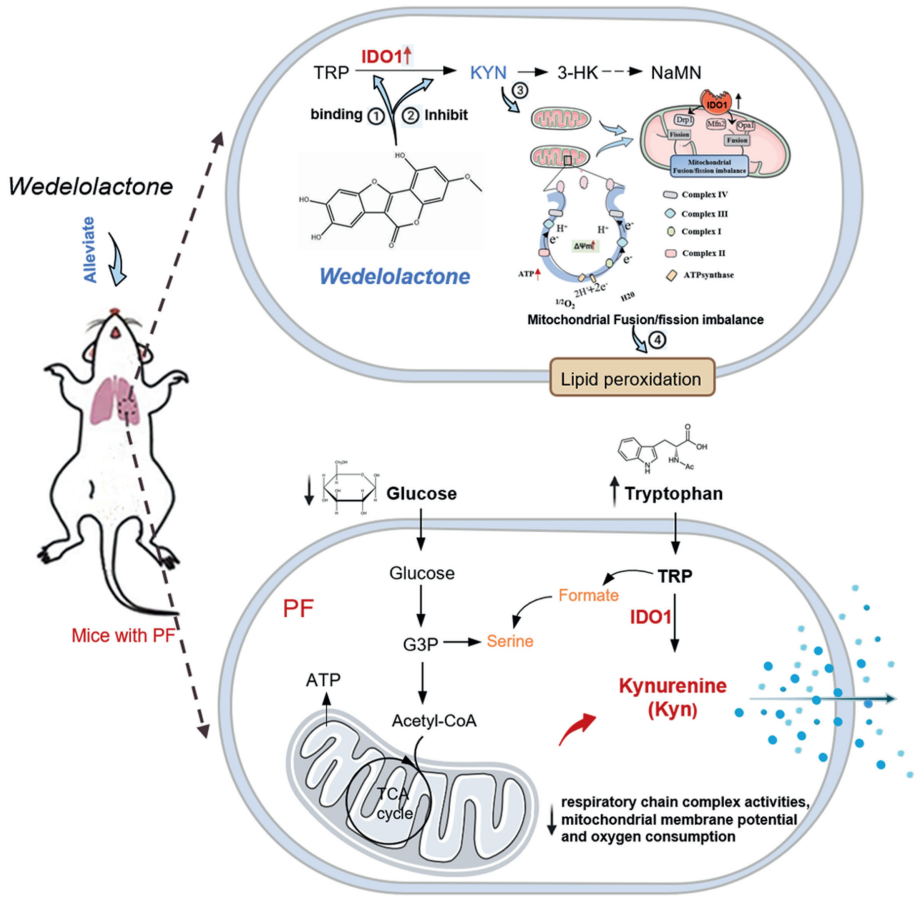

Figure 12 Targeting IDO1 by WEL effectively suppresses the progression of PF. (1) IDO1 is a direct cellular target of WEL. (2) Targeting IDO1 with WEL helps ameliorate kynurenine metabolic disorders. (3) Imbalances in the kynurenine pathway metabolism caused abnormal mitochondrial dynamics and mitochondrial dysfunction. (4) Disruption of mitochondrial dynamics could impair lipid metabolism during lung fibrosis.

5. Conclusions

In summary, this study highlights the potential role of IDO1 in promoting lung fibrosis and proposes targeting IDO1 as a therapeutic strategy for treating PF. Additionally, we discovered that the small molecule WEL acts as an inhibitor of IDO1 by interacting with amino acid residue K242. These results provide promising perspectives for treating PF by targeting IDO1 to ameliorate mitochondrial dysfunction and dysregulated fatty acid metabolism. WEL is considered a leading candidate for natural product drugs and the development of new IDO1 inhibitors (Fig. 12).

Acknowledgments

The authors would like to extend their heartfelt appreciation for the generous financial assistance from the National Natural Science Foundation of China under grant number 82374027.

Author contributions

Lei Wang: Writing − original draft, Visualization, Project administration, Investigation, Formal analysis, Data curation, Conceptualization. Shanchun Ge: Validation, Investigation. Ye Zhang: Formal analysis, Data curation. Deqin Feng: Investigation. Ting Zhu: Investigation. Louqian Zhang: Investigation. Chaofeng Zhang: Supervision, Resources, Project administration, Investigation, Conceptualization.

Conflicts of interest

The authors report no conflicts of interest.

Appendix A. Supporting information

Supporting information to this article can be found online at https://doi.org/10.1016/j.apsb.2025.04.027.

References

1. Lederer DJ, Martinez FJ. Idiopathic pulmonary fibrosis. *N Engl J Med* 2018;**378**:1811−23.
2. Singh A, Chakraborty S, Wong SW, Hefner NA, Stuart A, Qadir AS, et al. Nanoparticle targeting of de novo profibrotic macrophages mitigates lung fibrosis. *Proc Natl Acad Sci U S A* 2022;**119**: e2121098119.
3. George PM, Wells AU, Jenkins RG. Pulmonary fibrosis and COVID-19: the potential role for antifibrotic therapy. *Lancet Respir Med* 2020; **8**:807−15.

4. Kim HJ, Perlman D, Tomic R. Natural history of idiopathic pulmonary fibrosis. *Respir Med* 2015;**109**:661−70.
5. Hao M, Fu R, Tai J, Tian Z, Yuan X, Chen Y, et al. S1PR1 serves as a viable drug target against pulmonary fibrosis by increasing the integrity of the endothelial barrier of the lung. *Acta Pharm Sin B* 2023; **13**:1110−27.
6. Johnston CJ, Smyth DJ, Dresser DW, Maizels RM. TGF-β in tolerance, development and regulation of immunity. *Cell Immunol* 2016; **299**:14−22.
7. Munn DH, Mellor AL. Indoleamine 2,3 dioxygenase and metabolic control of immune responses. *Trends Immunol* 2013;**34**:137−43.
8. Jasperson LK, Bucher C, Panoskaltsis-Mortari A, Mellor AL, Munn DH, Blazar BR. Inducing the tryptophan catabolic pathway, indoleamine 2,3-dioxygenase (Ido), for suppression of graft-*versus*-host disease (GVHD) lethality. *Blood* 2009;**114**:5062−70.
9. Thaker AI, Rao MS, Bishnupuri KS, Kerr TA, Foster L, Marinshaw JM, et al. Ido1 metabolites activate β-catenin signaling to promote cancer cell proliferation and colon tumorigenesis in mice. *Gastroenterology* 2013;**145**:416−25.
10. Hennequart M, Pilotte L, Cane S, Hoffmann D, Stroobant V, Plaen E, et al. Constitutive Ido1 expression in human tumors is driven by cyclooxygenase-2 and mediates intrinsic immune resistance. *Cancer Immunol Res* 2017;**5**:695−709.
11. Kim NS, Torrez T, Langridge W. LPS enhances CTB-insulin induction of Ido1 and IL-10 synthesis in human dendritic cells. *Cell Immunol* 2019;**338**:32−42.
12. Babcock TA, Carlin JM. Transcriptional activation of indoleamine dioxygenase by interleukin 1 and tumor necrosis factor alpha in interferon-treated epithelial cells. *Cytokine* 2000;**12**:588−94.
13. Broekhuizen M, Klein T, Hitzerd E, de Rijke YB, Schoenmakers S, Sedlmayr P, et al. l-Tryptophan-induced vasodilation is enhanced in preeclampsia: studies on its uptake and metabolism in the human placenta. *Hypertension* 2020;**76**:184−94.
14. Orabona C, Pallotta MT, Volpi C, Fallarino F, Vacca C, Bianchi R, et al. SOCS3 drives proteasomal degradation of indoleamine 2,3-dioxygenase (Ido) and antagonizes Ido-dependent tolerogenesis. *Proc Natl Acad Sci U S A* 2008;**105**:20828−33.
15. Thomas SR, Terentis AC, Cai H, Takikawa O, Levina A, Lay PA, et al. Post-translational regulation of human indoleamine 2,3-dioxygenase activity by nitric oxide. *J Biol Chem* 2007;**282**:23778−87.
16. Cheong JE, Sun L. Targeting the Ido1/TDO2−KYN−AhR pathway for cancer immunotherapy—challenges and opportunities. *Trends Pharmacol Sci* 2018;**39**:307−25.
17. Liu Y, Liang X, Dong W, Fang Y, Lv J, Zhang T, et al. Tumor-repopulating cells induce PD-1 expression in $CD8^+$ T cells by transferring kynurenine and AhR activation. *Cancer Cell* 2018;**33**:480-94.e7.
18. Brandacher G, Perathoner A, Ladurner R, Schneeberger S, Obrist P, Winkler C, et al. Prognostic value of indoleamine 2,3-dioxygenase expression in colorectal cancer: effect on tumor-infiltrating T cells. *Clin Cancer Res* 2006;**12**:1144−51.
19. Selman M, King TE, Pardo A. Idiopathic pulmonary fibrosis: prevailing and evolving hypotheses about its pathogenesis and implications for therapy. *Ann Intern Med* 2001;**134**:136−51.
20. Chapman HA. Epithelial−mesenchymal interactions in pulmonary fibrosis. *Annu Rev Physiol* 2011;**73**:413−35.
21. Wang L, Zhu T, Feng D, Li R, Zhang C. Polyphenols from Chinese herbal medicine: molecular mechanisms and therapeutic targets in pulmonary fibrosis. *Am J Chin Med* 2022;**50**:1063−94.
22. Wynn TA, Ramalingam TR. Mechanisms of fibrosis: therapeutic translation for fibrotic disease. *Nat Med* 2012;**18**:1028−40.
23. Lee SM, Park HY, Suh YS, Yoon EH, Kim J, Jang WH, et al. Inhibition of acute lethal pulmonary inflammation by the Ido−AhR pathway. *Proc Natl Acad Sci U S A* 2017;**114**:E5881−90.
24. Mo C, Xie S, Liu B, Zhong W, Zeng T, Huang S, et al. Indoleamine 2,3-dioxygenase 1 limits hepatic inflammatory cells recruitment and promotes bile duct ligation-induced liver fibrosis. *Cell Death Dis* 2021;**12**:16.
25. Shi D, Wu X, Jian Y, Wang J, Huang C, Mo S, et al. USP14 promotes tryptophan metabolism and immune suppression by stabilizing Ido1 in colorectal cancer. *Nat Commun* 2022;**13**:5644.
26. Liu Y, Liang X, Yin X, Lv J, Tang K, Ma J, et al. Blockade of Ido−kynurenine−AhR metabolic circuitry abrogates IFN-γ-induced immunologic dormancy of tumor-repopulating cells. *Nat Commun* 2017;**8**:15207.
27. Du L, Xing Z, Tao B, Li T, Yang D, Li W, et al. Both Ido1 and TDO contribute to the malignancy of gliomas *via* the Kyn−AhR−AQP4 signaling pathway. *Signal Transduct Target Ther* 2020;**5**:10.
28. Mu C, Choudhary A, Mayengbam S, Barrett KT, Rho JM, Shearer J, et al. Seizure modulation by the gut microbiota and tryptophan−kynurenine metabolism in an animal model of infantile spasms. *EBioMedicine* 2022;**76**:103833.
29. Jiang ZM, Zeng SL, Huang TQ, Lin Y, Wang FF, Gao XJ, et al. Sinomenine ameliorates rheumatoid arthritis by modulating tryptophan metabolism and activating aryl hydrocarbon receptor *via* gut microbiota regulation. *Sci Bull (Beijing)* 2023;**68**:1540−55.
30. Duan RN, Yang CL, Du T, Liu A, Wang AR, Sun WJ, et al. Smek1 deficiency exacerbates experimental autoimmune encephalomyelitis by activating proinflammatory microglia and suppressing the Ido1−AhR pathway. *J Neuroinflammation* 2021;**18**:145.
31. Ouyang L, Yu C, Xie Z, Su X, Xu Z, Song P, et al. Indoleamine 2,3-dioxygenase 1 deletion-mediated kynurenine insufficiency in vascular smooth muscle cells exacerbates arterial calcification. *Circulation* 2022;**145**:1784−98.
32. Sadik A, Somarribas Patterson LF, Öztürk S, Mohapatra SR, Panitz V, Secker PF, et al. IL4I1 is a metabolic immune checkpoint that activates the AHR and promotes tumor progression. *Cell* 2020;**182**:1252-70.e34.
33. Chen B, Alvarado DM, Iticovici M, Kau NS, Park H, Parikh PJ, et al. Interferon-induced Ido1 mediates radiation resistance and is a therapeutic target in colorectal cancer. *Cancer Immunol Res* 2020;**8**: 451−64.
34. Duan Z, Zhang S, Liang H, Xing Z, Guo L, Shi L, et al. Amyloid β neurotoxicity is Ido1−Kyn−AhR dependent and blocked by Ido1 inhibitor. *Signal Transduct Target Ther* 2020;**5**:96.
35. Fujiwara N, Kubota N, Crouchet E, Koneru B, Marquez CA, Jajoriya AK, et al. Molecular signatures of long-term hepatocellular carcinoma risk in nonalcoholic fatty liver disease. *Sci Transl Med* 2022;**14**:eabo4474.
36. Ishak K, Baptista A, Bianchi L, Callea F, De Groote J, Gudat F, et al. Histological grading and staging of chronic hepatitis. *J Hepatol* 1995; **22**:696−9.
37. Adams TS, Schupp JC, Poli S, Ayaub EA, Neumark N, Ahangari F, et al. Single-cell RNA-seq reveals ectopic and aberrant lung-resident cell populations in idiopathic pulmonary fibrosis. *Sci Adv* 2020;**6**: eaba1983.
38. Zhao L, Zhu Y, Tao H, Chen X, Yin F, Zhang Y, et al. Ailanthone ameliorates pulmonary fibrosis by suppressing JUN-dependent MEOX1 activation. *Acta Pharm Sin B* 2024;**14**:3543−60.
39. Wang L, Wang J, Ren G, Sun S, Nishikawa K, Yu J, et al. Ameliorative effects of the Coptis inflorescence extract against lung injury in diabetic mice by regulating AMPK/NEU1 signaling. *Phytomedicine* 2023;**118**:154963.
40. Wang G, Cao K, Liu K, Xue Y, Roberts AI, Li F, et al. Kynurenic acid, an Ido metabolite, controls TSG-6-mediated immunosuppression of human mesenchymal stem cells. *Cell Death Differ* 2018;**25**:1209−23.
41. Bogaerts Y, Van Renterghem D, Vanvuchelen J, Praet M, Michielssen P, Blaton V, et al. Interstitial pneumonitis and pulmonary vasculitis in a patient taking an L-tryptophan preparation. *Eur Respir J* 1991;**4**:1033−6.
42. Christen S, Peterhans E, Stocker R. Antioxidant activities of some tryptophan metabolites: possible implication for inflammatory diseases. *Proc Natl Acad Sci U S A* 1990;**87**:2506−10.
43. Ogasawara N, Oguro T, Sakabe T, Matsushima M, Takikawa O, Isobe K, et al. Hemoglobin induces the expression of indoleamine 2,3-dioxygenase in dendritic cells through the activation of PI3K, PKC,

and NF-κB and the generation of reactive oxygen species. *J Cell Biochem* 2009;**108**:716−25.
44. Ju JM, Nam G, Lee YK, Jung M, Chang H, Kim W, et al. Ido1 scavenges reactive oxygen species in myeloid-derived suppressor cells to prevent graft-*versus*-host disease. *Proc Natl Acad Sci U S A* 2021; **118**:e2011170118.
45. Minhas PS, Liu L, Moon PK, Joshi AU, Dove C, Mhatre S, et al. Macrophage *de novo* NAD^+ synthesis specifies immune function in aging and inflammation. *Nat Immunol* 2019;**20**:50−63.
46. Chung KP, Hsu CL, Fan LC, Huang Z, Bhatia D, Chen YJ, et al. Mitofusins regulate lipid metabolism to mediate the development of lung fibrosis. *Nat Commun* 2019;**10**:3390.
47. Yi EY, Park SY, Jung SY, Jang WJ, Kim YJ. Mitochondrial dysfunction induces EMT through the TGF-β/Smad/Snail signaling pathway in Hep3B hepatocellular carcinoma cells. *Int J Oncol* 2015; **47**:1845−53.
48. Kumar S, Pan CC, Shah N, Wheeler SE, Hoyt KR, Hempel N, et al. Activation of Mitofusin2 by Smad2−RIN1 complex during mitochondrial fusion. *Mol Cell* 2016;**62**:520−31.
49. Du X, Duan M, Kan S, Yang Y, Xu S, Wei J, et al. TGF-β3 mediates mitochondrial dynamics through the p-Smad3/AMPK pathway. *Cell Prolif* 2024;**57**:e13579.
50. Qin MC, Li JJ, Zheng YT, Li YJ, Zhang YX, Ou RX, et al. Naringin ameliorates liver fibrosis in zebrafish by modulating Ido1-mediated lipid metabolism and inflammatory infiltration. *Food Funct* 2023;**14**: 10347−61.
51. Bridges JP, Ikegami M, Brilli LL, Chen X, Mason RJ, Shannon JM. LPCAT1 regulates surfactant phospholipid synthesis and is required for transitioning to air breathing in mice. *J Clin Investig* 2010;**120**: 1736−48.
52. Tian Y, Zhou R, Rehg JE, Jackowski S. Role of phosphocholine cytidylyltransferase alpha in lung development. *Mol Cell Biol* 2007; **27**:975−82.
53. Wu G, Aoyama C, Young SG, Vance DE. Early embryonic lethality caused by disruption of the gene for choline kinase alpha, the first enzyme in phosphatidylcholine biosynthesis. *J Biol Chem* 2008;**283**: 1456−62.
54. Li Y, Song Y, Deng G, Tan Q, Xu S, Yang M, et al. Indoleamine 2,3-dioxygenase 1 aggravates acetaminophen-induced acute liver failure by triggering excess nitroxidative stress and iron accumulation. *Free Radic Biol Med* 2021;**172**:578−89.
55. Ketelhuth DFJ. The immunometabolic role of indoleamine 2,3-dioxygenase in atherosclerotic cardiovascular disease: immune homeostatic mechanisms in the artery wall. *Cardiovasc Res* 2019;**115**: 1408−15.
56. Tran HQ, Shin EJ, Saito K, Tran TV, Phan DH, Sharma N, et al. Indoleamine-2,3-dioxygenase-1 is a molecular target for the protective activity of mood stabilizers against mania-like behavior induced by d-amphetamine. *Food Chem Toxicol* 2020;**136**:110986.
57. Puddu GM, Cravero E, Arnone G, Muscari A, Puddu P. Molecular aspects of atherogenesis: new insights and unsolved questions. *J Biomed Sci* 2005;**12**:839−53.
58. Nogueira-Recalde U, Lorenzo-Gómez I, Blanco FJ, Loza MI, Grassi D, Shirinsky V, et al. Fibrates as drugs with senolytic and autophagic activity for osteoarthritis therapy. *EBioMedicine* 2019;**45**: 588−605.
59. Chung KW, Lee EK, Lee MK, Oh GT, Yu BP, Chung HY. Impairment of PPARα and the fatty acid oxidation pathway aggravates renal fibrosis during aging. *J Am Soc Nephrol* 2018;**29**:1223−37.
60. Zhang J, Zhang M, Huo XK, Ning J, Yu ZL, Morisseau C, et al. Macrophage inactivation by small molecule wedelolactone *via* targeting sEH for the treatment of LPS-induced acute lung injury. *ACS Cent Sci* 2023;**9**:440−56.
61. Kobori M, Yang Z, Gong D, Heissmeyer V, Zhu H, Jung YK, et al. Wedelolactone suppresses LPS-induced caspase-11 expression by directly inhibiting the IKK complex. *Cell Death Differ* 2004;**11**: 123−30.
62. Oakley F, Teoh V, Ching ASG, Bataller R, Colmenero J, Jonsson JR, et al. Angiotensin II activates IκB kinase phosphorylation of RelA at Ser 536 to promote myofibroblast survival and liver fibrosis. *Gastroenterology* 2009;**136**:2334−44.e1.
63. Xie L, Hu K, Duo Y, Shimokawa T, Kumata K, Zhang Y, et al. Off-tumor Ido1 target engagements determine the cancer-immune set point and predict the immunotherapeutic efficacy. *J Immunother Cancer* 2021;**9**:e002616.
64. Lee SM, Kim CE, Park HY, Yoon EH, Won HJ, Ahn JM, et al. Aryl hydrocarbon receptor-targeted therapy for $CD4^+$ T cell-mediated idiopathic pneumonia syndrome in mice. *Blood* 2022;**139**:3325−39.